

Article

Influence of Organic Matter Thermal Maturity on Rare Earth Element Distribution: A Study of Middle Devonian Black Shales from the Appalachian Basin, USA

Shailee Bhattacharya ^{1,*}, Shikha Sharma ¹, Vikas Agrawal ¹, Michael C. Dix ², Giovanni Zanoni ³, Justin E. Birdwell ⁴, Albert S. Wylie, Jr. ⁵ and Tom Wagner ⁶

- ¹ Department of Geology and Geography, West Virginia University, 98 Beechurst Ave, Morgantown, WV 26506, USA; shikha.sharma@mail.wvu.edu (S.S.)
² Independent Researcher, 3414 Beauchamp Street, Houston, TX 77009, USA
³ RohmTek, 6721 Portwest Drive, Suite 100, Houston, TX 77024, USA
⁴ U.S. Geological Survey, Denver Federal Center, Box 25046 MS 977, Denver, CO 80225, USA; jbirdwell@usgs.gov
⁵ Independent Researcher, P.O. Box 380, Mohawk, MI 49950, USA
⁶ Coterra Energy Inc., 2000 Park Lane, Suite 300, Pittsburgh, PA 15275, USA; tom.wagner@coterra.com
* Correspondence: sb0215@mix.wvu.edu

Abstract: This study focuses on understanding the association of rare earth elements (REE; lanthanides + yttrium + scandium) with organic matter from the Middle Devonian black shales of the Appalachian Basin. Developing a better understanding of the role of organic matter (OM) and thermal maturity in REE partitioning may help improve current geochemical models of REE enrichment in a wide range of black shales. We studied relationships between whole rock REE content and total organic carbon (TOC) and compared the correlations with a suite of global oil shales that contain TOC as high as 60 wt.%. The sequential leaching of the Appalachian shale samples was conducted to evaluate the REE content associated with carbonates, Fe–Mn oxyhydroxides, sulfides, and organics. Finally, the residue from the leaching experiment was analyzed to assess the mineralogical changes and REE extraction efficiency. Our results show that heavier REE (HREE) have a positive correlation with TOC in our Appalachian core samples. However, data from the global oil shales display an opposite trend. We propose that although TOC controls REE enrichment, thermal maturation likely plays a critical role in HREE partitioning into refractory organic phases, such as pyrobitumen. The REE inventory from a core in the Appalachian Basin shows that (1) the total REE ranges between 180 and 270 ppm and the OM-rich samples tend to contain more REE than the calcareous shales; (2) there is a relatively higher abundance of middle REE (MREE) to HREE than lighter REE (LREE); (3) there is a disproportionate increase in Y and Tb with TOC likely due to the rocks being over-mature; and (4) the REE extraction demonstrates that although the OM has higher HREE concentration, the organic leachates contain more LREE, suggesting it is more challenging to extract HREE from OM than using traditional leaching techniques.

Keywords: rare earth elements; organic matter; thermal maturity; black shales; Appalachian Basin



Citation: Bhattacharya, S.; Sharma, S.; Agrawal, V.; Dix, M.C.; Zanoni, G.; Birdwell, J.E.; Wylie, A.S., Jr.; Wagner, T. Influence of Organic Matter Thermal Maturity on Rare Earth Element Distribution: A Study of Middle Devonian Black Shales from the Appalachian Basin, USA. *Energies* **2024**, *17*, 2107. <https://doi.org/10.3390/en17092107>

Academic Editors: Shu Tao, Dameng Liu, Wei Ju, Shida Chen, Zhengguang Zhang and Jiang Han

Received: 23 January 2024

Revised: 11 April 2024

Accepted: 14 April 2024

Published: 28 April 2024



Copyright: © 2024 by the authors. Licensee MDPI, Basel, Switzerland. This article is an open access article distributed under the terms and conditions of the Creative Commons Attribution (CC BY) license (<https://creativecommons.org/licenses/by/4.0/>).

1. Introduction

To meet the high demands for rare earth elements (REE) needed for energy transition technologies, recent and ongoing research has been focused on identifying and evaluating unconventional sources of REE like coal mine drainage and coal-related products such as refuse, coal-fired power plant ash, overburden, underclays, and, more recently, black shales [1]. The Appalachian Basin, situated in the eastern U.S., has been one of the largest producers of oil and natural gas in the last two decades [2,3]. This basin, which includes Middle Devonian black shales of varying total organic carbon (TOC) content and spatial

maturity, is an important exploration target for REE within the volume of waste material like shale cuttings from horizontally drilled oil and natural gas extraction wells. Our study is an attempt at understanding the modes of REE occurrence in the different phases of black and calcareous shales in the Appalachian Basin. While the modes of association with carbonates, sulfides, framework silicates, and clays are well documented [4,5], there is a lack of understanding regarding the role of organic matter (OM) in REE enrichment [5,6]. Furthermore, the linkage between the thermal maturity of shales and their elemental enrichment has also not been addressed adequately. Therefore, to our knowledge, this study is one of the first that attempts to develop an REE inventory in Middle Devonian black shales, with particular focus on developing a holistic geochemical model of REE distribution in the organic fraction, and finally, establishing a relationship between the thermal maturity of shales and REE enrichment.

2. Geochemical Background

2.1. Role of Organic Matter (OM) in REE Partitioning

Black shales preserve critical mineral deposits like transition metals and rare earth elements [7]. They also act as recorders of changes such as shifts in redox conditions, diagenetic processes, and thermal influences on mineral composition. REE are categorized into light (LREE) (La–Nd, Sc), middle (MREE) (Sm–Ho, Y), and heavy (HREE) (Er–Lu) using the scheme proposed by Yang et al., 2017 [5]. Variations in REE concentrations in rocks of different thermal maturities result from processes like element mobilization during catagenesis, the segregation of REE-rich mineral phases, and sediment mixing. Typically, rivers and seawater show an enrichment of MREE relative to HREE, except in cases of acidic waters with a pH below 7 [8–10]. Estuaries are a unique zone where a significant number of lanthanides are scavenged by suspended matter or complexed with Fe–Mn oxyhydroxides, which results in a decrease in REE concentration in seawater relative to rivers (10 times higher levels) [11]. In seawater, during the early stages of diagenesis, sedimentary OM, oxyhydroxides, and trace elements like REE, Th, U, and Pb may migrate to sediment porewaters. This can be due to sediment dewatering, clay mineral transformations, and Fe–Mn reduction, leading to the preferential release of incompatible elements [12–14]. When oxic degradation in OM occurs, REE are released in the order LREE > MREE > HREE due to increasing complexing efficiency across series with carbonate species [14–17]. As depth increases, this results in an increase in HREE concentration in seawater closer to the sediment–water interface, similar to those of trace elements that behave as micronutrients, such as vanadium (refer to Discussion Section 6.2). HREE enrichment in carbonate minerals may result from higher stability of HREE complexes with carbonate ions or similarity in ionic radius between heavy lanthanides and Ca^{2+} [9]. In samples without a positive correlation between Ca and HREE, it may be due to replacement of Ca by HREE [18]. Also, the rate of OM degradation significantly impacts the association of HREE with carbonates, as seen in Haley et al. (2004) [19], that may arise from factors such as episodic OM input, slower carbon burial rates, an increase in thermally labile OM contributions, or some combination of these. The relative changes in HREE and LREE content in sediment pores can vary with depth and geochemical processes at the sediment–water interface [19]. Ratios such as HREE/LREE or MREE/LREE emphasize fractionation processes to remove the effect of individual concentrations. At shallow depths (0–2 cm), while HREE is at higher levels due to stable complexations, LREE is released from particulate organic matter due to remineralization. At greater depths (2–4 cm), the incomplete remineralization of OM may decrease LREE mobility and relatively increase HREE concentration. This phenomenon explains the source of REE in oxic, suboxic, and anoxic seawaters in the absence of Fe-oxides [20]. However, OM has also been proposed to play a role in the absence of carbonate complexation. The REE profiles show a good correlation with redox-sensitive elements, such as Cu, that are known to be strongly associated with OM and organic ligands [21]. This suggests that OM might play a key role in concentrating REEs in mudstones (see Discussion Section 6.2).

Variations in OM sources, OM composition (Figure 1), and lithology can also affect the REE distribution prior to thermal maturation [22–30]. During the burial, diagenesis, and formation of authigenic minerals such as apatite, clay transformations can significantly change the source rock REE signatures. For example, apatite has a strong affinity for MREE and therefore acts as a sink for those elements only when the P_2O_5 content is greater than 0.5% [31]. Other minerals like authigenic clays and Fe–Mn oxyhydroxides can scavenge REE from highly enriched pore water. It is assumed that shale diagenesis occurs in closed systems and the overall rock chemistry remains the same even though the elemental compositions in individual mineralogical phases may differ from the source rock [18,32]. However, in nature, mudrocks or black shales can also act as open systems, leading to a significant loss or gain of old and new material, respectively [12,33,34]. At mildly high temperatures, humic acid production in the pores may increase, affecting the REE mobility and complicating the reconstruction of paleo-depositional environments ([18], and references therein).

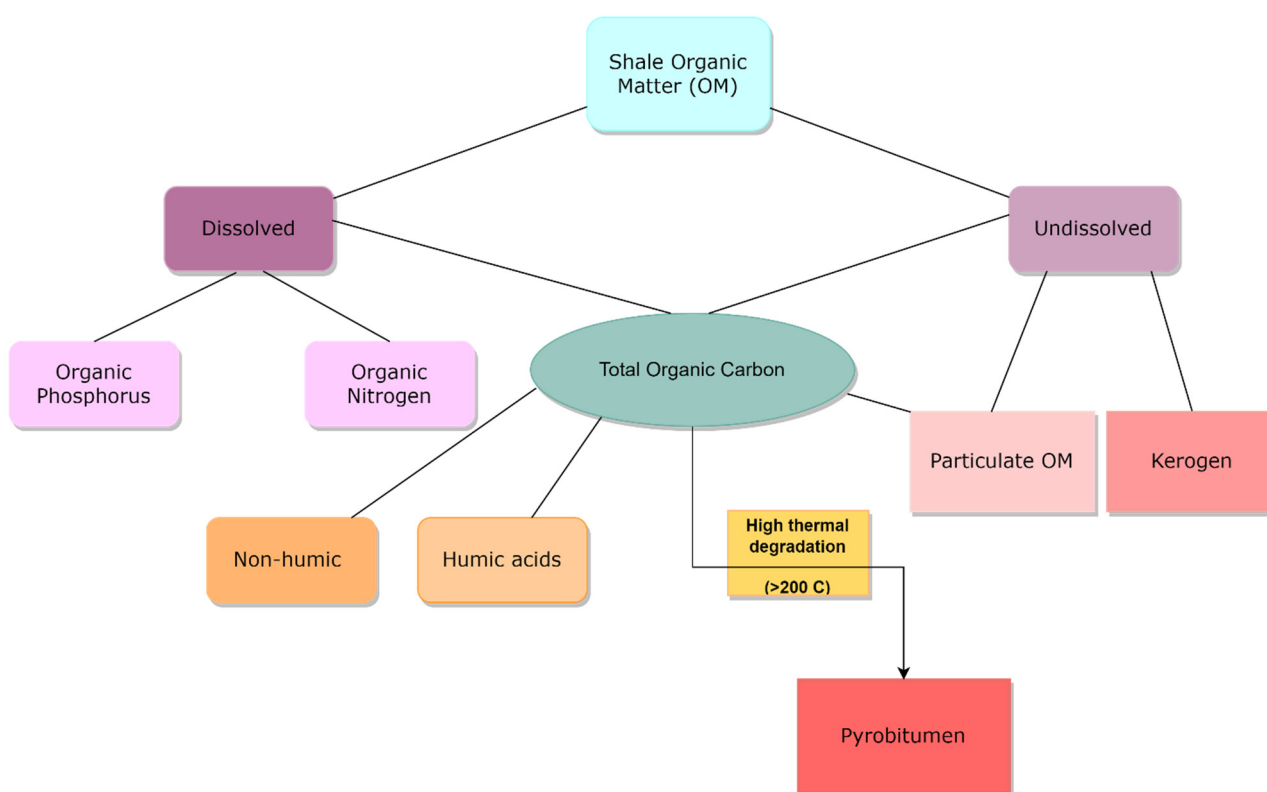


Figure 1. Constituents of shale organic matter.

2.2. Role of Thermal Maturity in HREE Partitioning

The process of thermal maturation significantly affects OM structure and can impact REE distribution. When thermal maturation progresses, OM loss may be significantly high [35], particularly for source rocks with high aliphatic carbon content [36]. The extent to which OM may be retained or lost during catagenesis was addressed in one of the pioneer studies conducted to explain the preservation of alkanes (or soluble OM) in highly mature Canadian black shales [37]. It is one of the first studies to have reported higher HREE abundance in mature black shales. The OM is found in three different forms: Insoluble remobilized bitumenite, insoluble in situ bitumenite, and soluble OM. Pyrobitumen is the type of insoluble solid bitumen (Figure 1) that represents the residue from oil, and it is generated at a later stage along with gas during the cracking of oil [38,39]. Soluble OM is expected to be eliminated from the shale at the onset of regional metamorphism [37]. The physical properties of the shale, such as the porosity, permeability, and alignment of the foliated minerals seem to be linked to controlling the amount of soluble OM retained in

the formation [37]. Photomicrographs of highly mature black shales demonstrate that the mobility of previously soluble bitumen and OM that is now insoluble pyrobitumen is due to the alignment of maximum permeability along foliated phyllosilicates in the direction perpendicular to that of the increasing diagenesis and metamorphism. Consequently, some alkanes were incorporated into recrystallizing minerals such as phyllosilicates, during the generation of pyrobitumen associated with increased maturation. While OM characterization is beyond the scope of this work, it is plausible that the rocks in our study area have been subjected to similar geological processes due to their high maturation (see Discussion Section 6.1).

In xenotime, Y is known to occur at the interstices of pyrobitumen nodules and may also be present either in the structure or occur as nanoparticles [40]. The HREE in general tend to be more abundant in pyrobitumen than LREE. A detailed micro-particle induced X-ray emission (μ PIXE) study of massive pyrobitumen isolates indicate the presence of HREE in the structure or as nanoparticles [40]. Recent advances in research on tetrapyrrolic and porphyrin complexes demonstrate that the heavier lanthanides and Y have strong hydrophilic properties [41]. These compounds are critical in the context of our study as it has been long known that high concentrations of Ni and V in crude oils are because of their ability to form tetrapyrrole complexes [42] that have high thermal stability [43,44], resistance to strong acids [45,46], and inertness to cation exchange reactions [47]. Furthermore, the high tenacity of tetrapyrrolic compounds is enhanced by metalation, bivalency, and small ionic radii, and all three factors are conveniently satisfied by Ni and V [43,45,48–51]. Conversely, owing to the large ionic radii and high coordination numbers, REE are also well-suited to form sandwich double- and triple-decker complexes with porphyrins, phthalocyanines, and related macrocycles [40,41,52–56]. The most favorable conditions in accumulating sediments for such bonding to occur are a reducing ($E_h < 0$) and anaerobic environment that supports tetrapyrrole preservation [57–59].

3. Geology of Study Area

The Appalachian Basin represents a continuous stratigraphic sequence in the eastern U.S. spanning a large area across several states [60–66]. The Middle Devonian sequence was deposited in an asymmetric foreland basin (Figure 2) [67] during the Acadian orogeny. During deposition, there were intermittent stages of active volcanism and quiescence, characterized by layers of volcanic materials and trace elemental proxies, such as Th, Rb, Cs, Ta, and LREE [68]. Organic-rich black shales were deposited during periods of reduced sediment influx into the Appalachian Basin due to its distal location. Besides the prevailing tectonic influences, rising sea level is considered the dominant factor controlling Middle Devonian black shale deposition. Three major tectophases occurred in the Devonian. The second tectophase (Eifelian–early Givetian) triggered the deposition of the Marcellus Shale, which marked an abrupt transition from the Onondaga Limestone platform [69]. This lithological transition is attributed to the combined effect of rapid subsidence due to tectonic loading and eustatic sea level rise [61]. Furthermore, various studies using proxies such as concentrations of Mo and U, degree of pyritization, Mo and S isotopes, rare earth patterns in organic-rich and organic-lean sections, and I/Ca ratio in sediments have concluded that these black shales or mudrocks were deposited under fluctuating redox conditions [60,63,70–78]. As the orogeny advanced in the craton-ward direction, the organic-rich sediment underwent clastic dilution, and the deposits became successively poorer in carbonates and OM.

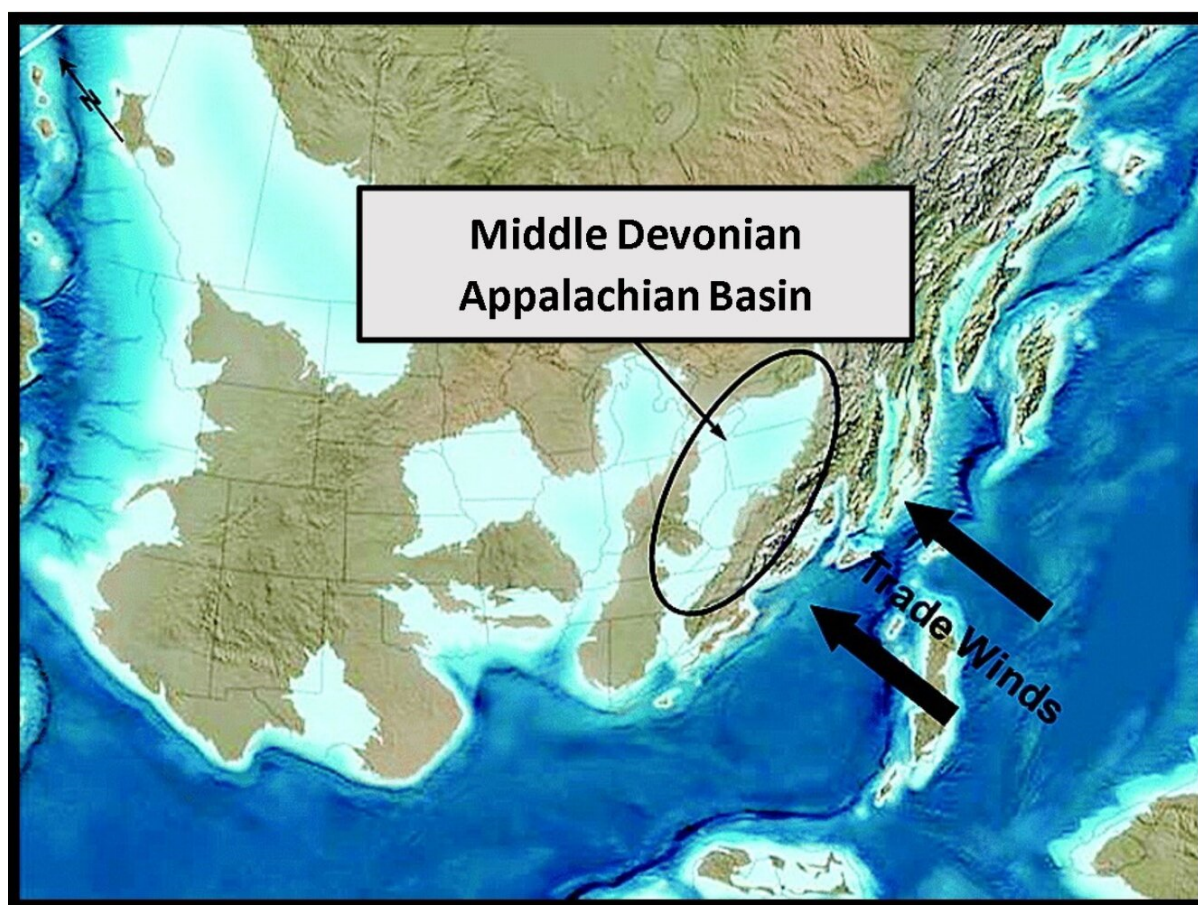


Figure 2. Paleogeographic map during the Middle Devonian (385 Ma) Acadian orogeny. Black oval indicates the general location of the study area; black arrows indicate paleo-wind direction. Modified from Blakey, 2005 [79].

The current stratigraphic divisions link the fine-grained Marcellus subgroup of the distal western margin of the basin with the proximal eastern basin such that the Marcellus Shale is defined as a part of a generally shallowing upwards trend of basinal black shale to nearshore sandstone and alluvial deposits [80–82]. The Purcell member of the Marcellus Shale comprises bedded and nodular fine-grained limestone [80,81]. The limestone occurs between the upper and lower Marcellus subgroups above the Union Springs member of the Marcellus Shale but is relatively thinner than the black shales. The Union Springs member at the base of the lower Marcellus subgroup above the Onondaga platform is characterized by the black shale of the Shamokin member of the Marcellus Shale [81]. The Union Springs basal section exhibits exceptionally high radioactivity and low density, and is composed of quartz, pyrite, TOC, and lower clay content [81]. In contrast, the upper part of the formation reports a less prominent radioactive response and increased bulk density due to relatively lower OM content and a higher content of framework silicates [83].

4. Materials and Methods

The samples given in Table 1 were collected from a cored well in the Appalachian Basin (exact well location and stratigraphic unit names and depth information are proprietary). The general location is represented in Figure 2. These samples are labeled from A1 (bottom-most) to D1 (topmost) in decreasing order of depth. A few samples have the same identifier suggesting that those were collected from different depths of a particular formation. For example, the first A2 sample at the bottom of Table 1 is a deeper sample than the overlying A2. To screen the samples and identify an appropriate set for this study, preliminary elemental concentrations were obtained using energy dispersive-X-ray fluorescence (ED-XRF;

hand-held Bruker Tracer 5i) from the slab core face at 1.0-inch intervals. TOC and total sulfur values were determined using Leco analyzer from the powders drilled from the back of the cores and from the same depths as the ED-XRF measurements. All data thus obtained in this study correspond to the same depths and intervals. This study comprises ten core samples (plugs and segments) that were stratigraphically above, below, and from the Marcellus Shale (Table 1) and belong to the dry gas window. The samples were homogenized to 75 μm at the Premier Corex Laboratory and sent to West Virginia University (Morgantown, WV, USA) for whole rock analyses and sequential leaching experiments.

Table 1. General description of the core samples.

| Sample Identifier | Lithofacies | Sample Type |
|-------------------|----------------|---|
| D1 | Clay-rich | 1.5-inch plug, center depth (Upper) |
| D1 | Clay-rich | 1.5-inch plug, center depth (Lower) |
| C3 | Clay-rich | 1.5-inch plug and laterally adjacent core segment |
| C2 | Carbonate-rich | 1.5-inch plug, center depth |
| C1 | Carbonate-rich | 1.5-inch plug, center depth |
| B | Organic-rich | 1.5-inch plug, center depth (Upper) |
| B | Organic-rich | 1.5-inch plug, center depth (Lower) |
| A2 | Organic-rich | 1.5-inch plug, center depth (Upper) |
| A2 | Organic-rich | core segment (Lower) |
| A1 | Carbonate-rich | core segment |

Mineralogical characterization of the samples was conducted at the Premier Corex Laboratory through X-ray diffraction (XRD). The XRD analysis was carried out on the bulk-rock fraction using a Bruker D8 Advance instrument. Initial preparation of bulk-rock samples involved powdering the material in a McCrone mill and side-loading before conducting bulk-rock measurements. Subsequently, clay analysis was performed following the separation of the clay fraction using centrifugation, adhering to the company's proprietary workflow. The measurement parameters included a step scan in the Bragg–Brentano geometry employing $\text{CuK}\alpha$ radiation (40 kV and 30 mA). For both bulk-rock and clay fraction, samples were scanned at a counting time of 1.8 s per $0.02^\circ 2\theta$, from 3 to $70^\circ 2\theta$, and 1 s per $0.02^\circ 2\theta$ from 3 to $30^\circ 2\theta$, for bulk-rock and clay fraction, respectively. Mineral phase interpretation and quantification were achieved using the Reference Intensity Ratio method, calibrated with in-house artificial mixes.

For the Sequential leaching procedure, 10 g of a sample (75 μm) was first washed with 150 mL of deionized (DI) water in a 400 mL borosilicate beaker and rolled for 18 h on an orbital shaker. The fluid was filtered using a 0.45 μm Millipore membrane filter. Following this, reagents were added to sequentially extract the inorganic and organic fractions from the shale. First, 80 mL of 1 M magnesium chloride was used to dissolve the exchangeable fraction. Second, the carbonates and phosphates were targeted using 150 mL of 1 N acetic acid, and constant shaking for 6 h at room temperature. Next, the Fe–Mn oxyhydroxides were dissolved using 150 mL of 0.05 M hydroxylamine hydrochloride in 25% acetic acid for 6 h at pH 2. Following the oxyhydroxides, pyrite was dissolved in 150 mL of 2 M nitric acid by constant shaking for 18 h at room temperature. The final step was designed to target the organically associated particles. First, the sample residue remaining after pyrite dissolution was combusted in a furnace at 650°C in porcelain crucibles for 3 h to oxidize the organics. This step was performed to ensure the REE would be concentrated as rare earth oxides in the burnt residue that is predominantly a refractory material, i.e., silicates. After combustion, the sample was washed in 150 mL of 0.1 M HCl and shaken for 4 h to separate the REE from the residue. The supernatant fluids formed after every leaching step were collected by vacuum filtering using 0.45 μm membrane filters and subsequently acidified with 1% conc. nitric acid to prevent chemical deterioration of the sample. Additionally, the sample residue after each leaching step was washed in 150 mL of DI water, collected, and acidified for future analyses (if necessary) to account for the elemental loss in between the leaching steps.

About 5 g of each powdered shale sample was used for whole-rock digestion by the sodium peroxide fusion method. Major and trace element concentrations were measured in acidified leachates and whole-rock concentrations using EPA methods 200.7 and a modified 200.8, respectively [84,85]. These steps were taken to ensure analytical accuracy and reproducibility following QA/QC protocol. The instrument was run daily with four points and a blank along with a positive and a negative check. The positive check was to ensure recoveries were proper. The negative check (or the continuing blank) was performed to ensure that the blank was below the method detection limit (MDL). Check standards were run after every 10 injections to ensure that the analytical uncertainty was within $\pm 10\%$ for the calibration verification standard, and calibration blank standards were run every 10 samples. Each batch of 20 samples had a batch blank and laboratory control spike in addition to one sample run in duplicate. The MDLs for the elements are provided in the Supplementary Materials.

Kerogen isolation was performed on pulverized aliquots of the oil shale samples using a sequential acid treatment method [86]. Initially, 18% *w/w* hydrochloric acid was added to the samples to remove carbonate minerals, followed by 52% *w/w* hydrofluoric acid to remove aluminosilicates, and then boiling 37% *w/w* hydrochloric acid was used to remove fluorosilicates produced by the hydrofluoric acid treatment. After removal of residual acid with multiple washes using deionized water, a heavy-liquid separation was performed in a zinc bromide solution to reduce pyrite and other heavy acid-resistant minerals. Additional hot HCl treatments to remove minerals like ralsstonite (evaluated by qualitative X-ray diffraction analysis) were employed when required. Finally, a Soxhlet extraction of the organic isolate using a 60:40 (wt%) benzene-methanol azeotrope was employed to remove any residual ZnBr_2 and extractable OM. Kerogen samples were then dried in a vacuum oven overnight (60 °C). Major and trace element analyses were performed on whole rock powders and kerogen isolates (after ashing) by SGS Laboratories (Toronto, Canada) using an inductively coupled plasma-optical emission spectroscopy-mass spectroscopy (ICP-OES-MS) method following preparation of samples by sodium peroxide fusion [87].

5. Results

5.1. General Mineralogical Information of the Shale Samples

In our investigation, the mineralogical results in Table 2 and Figure 3 show that samples are typically organic-rich mudrocks and have a moderate to high amount of quartz (19.3–34.0%), feldspar (Plag + Kfsp) (4.7–7.4%), total clay (illite/mica + chlorite) (13.3–60.1%), carbonates (Cal + Dol + Fe-Dol) (1.2–60.7%), pyrite (1.4–6.5%), and TOC (0.41–8.73%). Other minerals were anatase (0.5–1.1%) and barite (trace amount). The TOC increases in the interval between D1 and C2, decreasing sharply at C1, before increasing substantially in the lower horizons until reaching 4.90% at A1, which is a carbonate platform with 53.5% calcite. Other horizons that are carbonate-rich but relatively less in TOC are C2 and C1 (CaCO_3 = 19.5% and 35.8% respectively). The TOC-rich zones are concentrated in the lower portion of the core found in three horizons, namely B and A2.

Table 3 provides the major elemental contents as oxides that constitute the major shale-forming minerals. The siliciclastic indicators, namely, SiO_2 ranges from 34.26 wt% in A1 to 60.14 wt% in D1, TiO_2 from 0.24 wt% to 0.78 wt% in D1, Al_2O_3 from 4.42 wt% in A1 to 16.35 wt% in D1, Na_2O 0.63 wt% in A1 to 1.12 wt% in upper B, and K_2O from 0.82 wt% in A1 to 4.15 wt% in the upper D1 sample. Pyrite is represented by Fe_2O_3 ranging from 1.61 wt% in A1 to 7.52 wt% in lower D1 and total sulfur from 0.83 wt% in C2 to 4.06 wt% in lower B, which is also the sample with highest pyrite content. Carbonates are constituted of CaO , ranging from 0.97 wt% in D1 to 25.19 wt% in A1, and MgO from 0.92 wt% in A2 to 3.04 wt% in C1.

Table 2. XRD-determined mineralogical content and Leco-TOC of core samples.

| ID | Qtz | Plag | Kfsp | Ill/Mic | Chl | Cal | Dol | Fe-Dol | Pyr | Bar | Anat | TOC |
|----|------|------|------|---------|-----|------|-----|--------|-----|-----|------|------|
| | % | % | % | % | % | % | % | % | % | % | % | % |
| D1 | 27.9 | 5.6 | 0.5 | 52.4 | 7.7 | 0.6 | 0.6 | 0.0 | 2.5 | 0.0 | 1.1 | 1.90 |
| D1 | 30.6 | 6.0 | 0.4 | 45.7 | 5.6 | 1.4 | 0.3 | 1.1 | 5.9 | 0.0 | 1.1 | 3.37 |
| C3 | 29.0 | 6.8 | 0.3 | 40.1 | 3.1 | 13.6 | 1.4 | 4.5 | 1.8 | 0.0 | 1.1 | 4.18 |
| C2 | 19.3 | 5.4 | 0.4 | 38.2 | 0.9 | 30.5 | 3.7 | 1.6 | 1.4 | 0.0 | 0.7 | 3.27 |
| C1 | 24.6 | 6.0 | 0.3 | 37.7 | 1.0 | 26.7 | 8.8 | 11.0 | 2.5 | 0.0 | 0.8 | 0.41 |
| B | 27.2 | 7.4 | 0.0 | 42.1 | 1.6 | 11.0 | 4.2 | 1.7 | 4.5 | 0.0 | 0.6 | 5.63 |
| B | 30.3 | 6.7 | 0.0 | 34.8 | 0.0 | 12.3 | 1.3 | 0.6 | 6.5 | 0.0 | 0.7 | 8.69 |
| A2 | 26.8 | 6.5 | 0.0 | 22.5 | 0.0 | 30.0 | 1.4 | 0.3 | 4.7 | 0.0 | 0.7 | 8.73 |
| A2 | 34.0 | 6.7 | 0.0 | 16.9 | 0.0 | 29.4 | 5.8 | 0.3 | 5.5 | 0.0 | 0.7 | 6.75 |
| A1 | 21.1 | 4.7 | 0.0 | 13.3 | 0.0 | 53.5 | 6.2 | 1.0 | 2.0 | 0.0 | 0.5 | 4.90 |

Qtz: Quartz; Plag: Plagioclase feldspar; Kfsp: K-Feldspar; Ill/Mic: Illite/Mica; Chl: Chlorite; Dol: Dolomite; Pyr: Pyrite; Bar: Barite; Anat: Anatase; %: weight percent.

Table 3. Major elemental content of the whole rock.

| Sample ID | SiO ₂ | TiO ₂ | Al ₂ O ₃ | Fe ₂ O ₃ | MnO | MgO | CaO | Na ₂ O | K ₂ O | P ₂ O ₅ | Leco S | BaO |
|-----------|------------------|------------------|--------------------------------|--------------------------------|------|------|-------|-------------------|------------------|-------------------------------|--------|------|
| | % | % | % | % | % | % | % | % | % | % | % | % |
| D1 | 59.02 | 0.78 | 16.35 | 6.37 | 0.03 | 1.70 | 0.97 | 1.05 | 4.15 | 0.08 | 1.59 | 0.25 |
| D1 | 60.14 | 0.69 | 14.24 | 7.52 | 0.03 | 1.45 | 1.24 | 1.07 | 3.70 | 0.09 | 3.90 | 0.37 |
| C3 | 53.10 | 0.54 | 11.91 | 3.64 | 0.03 | 1.87 | 6.99 | 1.10 | 3.09 | 0.05 | 1.10 | 0.24 |
| C2 | 40.76 | 0.57 | 11.22 | 2.63 | 0.03 | 1.60 | 16.77 | 0.89 | 2.91 | 0.04 | 0.83 | 0.26 |
| C1 | 46.35 | 0.63 | 11.21 | 5.74 | 0.07 | 3.04 | 10.63 | 1.00 | 2.65 | 0.13 | 1.87 | 0.36 |
| B | 55.14 | 0.63 | 13.08 | 5.24 | 0.03 | 1.43 | 4.81 | 1.12 | 3.43 | 0.09 | 2.55 | 0.36 |
| B | 52.42 | 0.49 | 10.37 | 5.57 | 0.02 | 1.06 | 6.67 | 1.08 | 2.65 | 0.10 | 4.06 | 0.29 |
| A2 | 41.48 | 0.32 | 6.92 | 3.80 | 0.02 | 0.92 | 16.64 | 1.01 | 1.90 | 0.09 | 2.84 | 0.16 |
| A2 | 45.75 | 0.28 | 5.45 | 5.45 | 0.02 | 1.89 | 15.42 | 0.78 | 1.21 | 0.10 | 3.91 | 0.12 |
| A1 | 34.26 | 0.24 | 4.42 | 1.61 | 0.01 | 2.07 | 25.19 | 0.63 | 0.82 | 0.11 | 1.05 | 0.14 |

5.2. Rare Earth Elements in the Whole Rock

The individual REE contents in the whole rock are given in Table 4. We further categorized these elements into light (LREE) (La–Nd, Sc), middle (MREE) (Sm–Ho, Y), and heavy (HREE) (Er–Lu) using the scheme proposed by [5]. The Total REE (TREE) content is consistently higher in the black shales than in the calcareous shales. The increasing trend in REE content from the base to the top section coincides with an increase in Al₂O₃ and TiO₂ as well as SiO₂ and K₂O. However, when grouped into light, middle, and heavy, there are more distinct relationships observed as given in the heat map in Table 5.

Table 4. Individual and total REE content in the whole rock and PAAS.

| ID | Sc | Y | La | Ce | Pr | Nd | Sm | Eu | Gd | Tb | Dy | Ho | Er | Tm | Yb | Lu | TREE |
|------|------|------|------|------|------|------|-----|------|------|-----|------|------|-----|-----|-----|-----|-------|
| | ppm | ppm | ppm | ppm | ppm | ppm | ppm | ppm | ppm | ppm | ppm | ppm | ppm | ppm | ppm | ppm | ppm |
| D1 | 16.7 | 25.0 | 44.5 | 90.2 | 10.6 | 40.9 | 7.5 | 1.63 | 7.5 | 1.1 | 6.8 | 1.40 | 3.9 | 0.6 | 3.7 | 0.6 | 262.5 |
| D1 | 13.2 | 24.9 | 45.3 | 89.6 | 11.3 | 44.9 | 9.4 | 2.07 | 9.2 | 1.4 | 7.5 | 1.55 | 4.4 | 0.7 | 4.3 | 0.6 | 270.3 |
| C3 | 13.4 | 18.7 | 37.0 | 72.1 | 9.2 | 35.6 | 6.7 | 1.39 | 6.5 | 0.9 | 5.1 | 1.08 | 3.2 | 0.4 | 2.9 | 0.6 | 214.7 |
| C2 | 11.9 | 18.9 | 38.6 | 73.3 | 9.3 | 35.1 | 5.9 | 1.28 | 6.1 | 0.8 | 5.1 | 0.99 | 2.9 | 0.4 | 2.9 | 0.4 | 213.8 |
| C1 | 10.5 | 15.2 | 33.0 | 65.5 | 7.8 | 29.7 | 5.8 | 1.40 | 6.1 | 0.9 | 5.2 | 1.02 | 2.8 | 0.4 | 2.7 | 0.4 | 188.5 |
| B | 13.6 | 24.4 | 40.4 | 78.8 | 9.8 | 38.6 | 7.7 | 1.97 | 8.1 | 1.2 | 7.2 | 1.47 | 4.2 | 0.6 | 3.8 | 0.4 | 242.2 |
| B | 13.5 | 29.8 | 39.2 | 73.7 | 9.8 | 39.5 | 8.6 | 2.03 | 9.4 | 1.4 | 8.2 | 1.68 | 4.7 | 0.7 | 4.3 | 0.6 | 247.1 |
| A2 | 11.4 | 56.5 | 39.1 | 58.9 | 9.2 | 39.1 | 8.9 | 2.24 | 11.2 | 1.7 | 10.0 | 2.20 | 6.2 | 0.9 | 5.6 | 0.6 | 264.1 |
| A2 | 11.9 | 34.7 | 28.9 | 46.7 | 7.9 | 32.5 | 6.7 | 1.54 | 7.6 | 1.1 | 6.8 | 1.35 | 4.0 | 0.6 | 3.8 | 0.9 | 196.7 |
| A1 | 7.7 | 26.6 | 23.9 | 33.0 | 5.3 | 21.3 | 4.7 | 1.07 | 6.0 | 0.9 | 5.2 | 1.08 | 2.9 | 0.4 | 2.6 | 0.5 | 143.2 |
| PAAS | 15.9 | 27.3 | 44.6 | 88.3 | 10.2 | 37.3 | 6.9 | 1.2 | 6.0 | 0.9 | 5.3 | 1.1 | 3.1 | 0.5 | 3.0 | 0.4 | 252.0 |

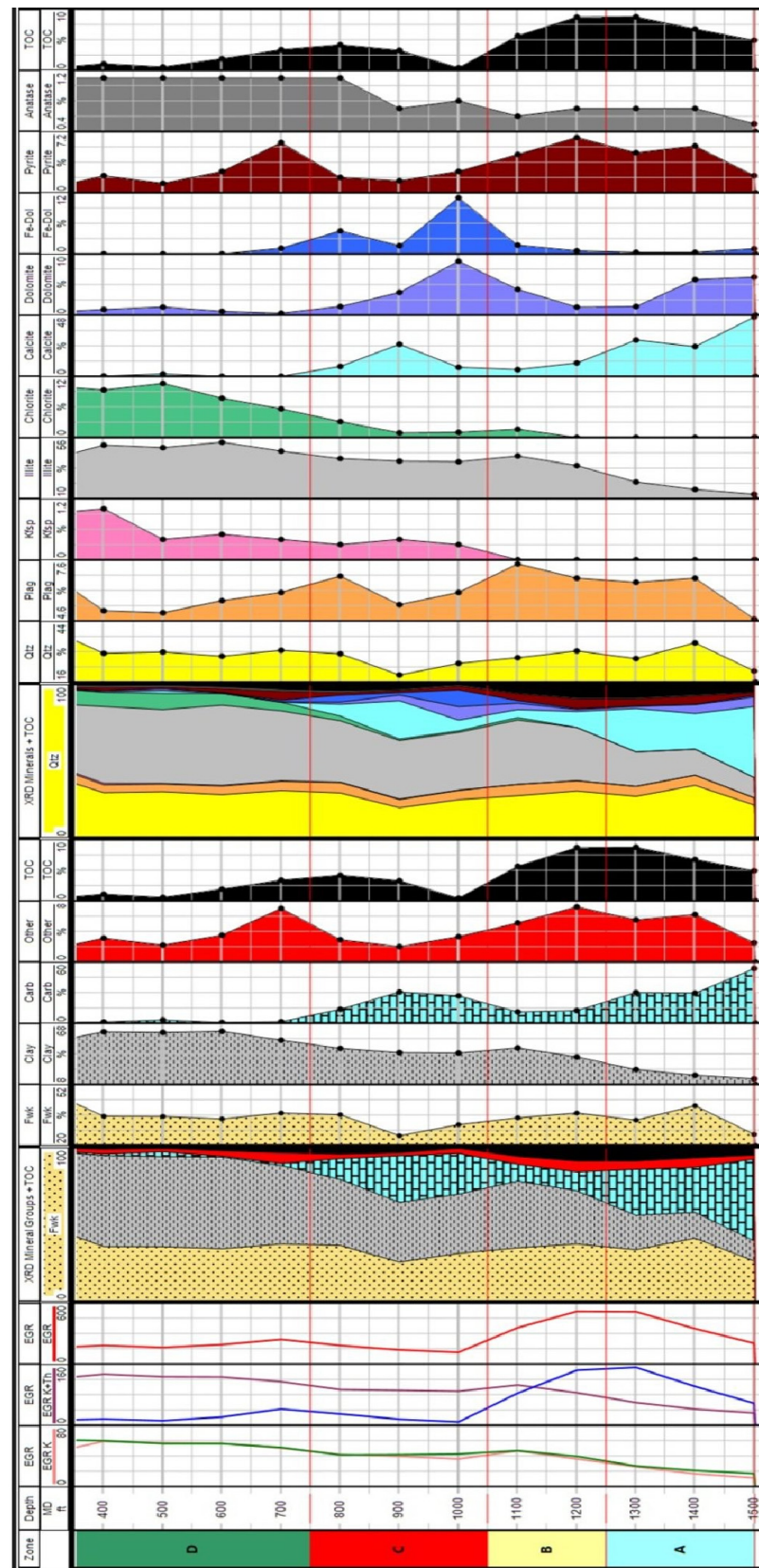


Figure 3. XRD-determined mineralogical proportions of the lithologic units of our study. The dominant groups comprising the whole shale are the siliciclastic, carbonates, mica clays, and pyrite and TOC.

Table 5. Heat map illustrating the relationship between the major shale phases and the REE groups.

| ID | SiO ₂ | TiO ₂ | Al ₂ O ₃ | K ₂ O | CaO | Chlorite | LREE (La–Nd) | Leco S | Leco Bulk TOC | HREE (Tb–Lu) |
|----|------------------|------------------|--------------------------------|------------------|-------|----------|-----------------|--------|------------------|-----------------|
| | % | % | % | % | % | % | ppm | % | % | ppm |
| D1 | 59.02 | 0.78 | 16.35 | 4.15 | 0.97 | 7.7 | 186.11 | 1.59 | 1.9 | 18.04 |
| D1 | 60.14 | 0.69 | 14.24 | 3.70 | 1.24 | 5.6 | 191.09 | 3.90 | 3.37 | 20.35 |
| C3 | 53.10 | 0.54 | 11.91 | 3.09 | 6.99 | 3.1 | 153.95 | 1.10 | 4.18 | 14.09 |
| C2 | 40.76 | 0.57 | 11.22 | 2.91 | 16.77 | 0.9 | 156.25 | 0.83 | 3.27 | 13.48 |
| C1 | 46.35 | 0.63 | 11.21 | 2.65 | 10.63 | 1.0 | 136.03 | 1.87 | 0.413 | 13.37 |
| B | 55.14 | 0.63 | 13.08 | 3.43 | 4.81 | 1.6 | 167.55 | 2.55 | 5.63 | 18.95 |
| B | 52.42 | 0.49 | 10.37 | 2.65 | 6.67 | 0.0 | 162.13 | 4.06 | 8.69 | 21.61 |
| A2 | 41.48 | 0.32 | 6.92 | 1.90 | 16.64 | 0.0 | 146.24 | 2.84 | 8.73 | 27.66 |
| A2 | 45.75 | 0.28 | 5.45 | 1.21 | 15.42 | 0.0 | 116.03 | 3.91 | 6.75 | 18.21 |
| A1 | 34.26 | 0.24 | 4.42 | 0.82 | 25.19 | 0.0 | 83.50 | 1.05 | 4.9 | 13.34 |

Min. values indicated in white. Max. values indicated in red.

The heat map in Table 5 demonstrates the covariation of the major inorganic and organic phases in our samples with LREE (La–Nd) and HREE (Tb–Lu), respectively. The numbers are assigned a white-red color gradient to represent the relative concentration of the sample in SiO₂, K₂O, TiO₂ (indicative of siliciclastic minerals), chlorite, CaO (calcite), S (sulfides), and TOC. The reason for excluding the Sc and Y from the grouping was to evaluate if these elements behaved similar to or different than a particular REE group. The two uppermost samples (D1) have the highest siliciclastic contents which corresponds with the highest LREE contents, followed by B and C3. The least silicate input is found in the carbonaceous shales that are C2, C1, A2, and A1. We found that the siliciclastic indicators for minerals like quartz, feldspar, and total clays show an affinity for LREE. On the other hand, S and TOC show a clear association with elevated Y and HREE from C1 down. This illustrates that although the REE have a preferential mode of enrichment into different inorganic species, the classical grouping needs further modification to better constrain the behavior of individual REE. This classification can be defined by chemical properties such as the nature of electronic orbitals and the specific electron interactions between particular types of REE and the phases in which they are enriched.

Figure 4 shows the Post-Archean Australian Shale (PAAS)-normalized [88] rare earth distribution in the whole rock with a moderately MREE to HREE-enriched pattern. Using the REE classification from [5], the MREE category includes six lanthanides (Sm, Eu, Gd, Tb, Dy, and Ho). However, in this study, it is evident that a transition in REE abundance starts at Tb. Hence, for a better understanding of the behavior of the heavy lanthanides, we hereby group the HREE from Tb to Lu. The Ce and Eu anomalies [9,89] were calculated as follows:

$$\text{Ce/Ce}^* = 2\text{Ce}_{\text{SN}} / (\text{La}_{\text{SN}} + \text{Pr}_{\text{SN}}) \quad (1)$$

$$\text{Eu/Eu}^* = 2\text{Eu}_{\text{SN}} / (\text{Sm}_{\text{SN}} + \text{Gd}_{\text{SN}}) \quad (2)$$

The anomalies in our samples occur as expected in black shales formed in deep ocean anoxic to suboxic basins (see Supplementary Materials, Table S1). There is significantly higher levels of Y relative to PAAS in the four deepest samples, i.e., one A1, two A2, and one B. The rest of the samples show a depletion in Y relative to PAAS, indicating that the source of Y higher up in the lithologic sections was either absent or these rocks may have undergone post-depositional changes to remove Y. We also observed a similar Tb enrichment, but, in this case, it is present in all samples relative to PAAS. It is likely that the modes of Y and Tb enrichment are similar, but during diagenesis, these elements can respond differently to fluid conditions.

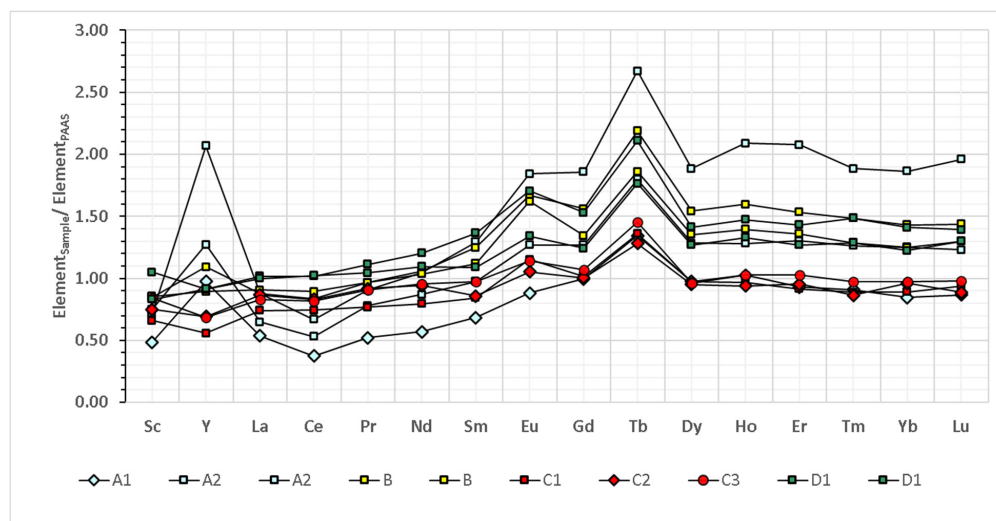


Figure 4. PAAS-normalized REE abundance in the 10 Middle Devonian shales.

5.3. Rare Earth Elements in the Organic Leachate

The ICP-determined concentration of individual rare earth elements extracted from organic leachate fraction and the total REE are given in Table 6. The total concentration extracted varies from only 0.62 to 6 ppm, indicating that a significant amount remained in the silicate residue. The LREE had higher levels in the leachates, followed by the MREE and the HREE. However, the multi-element graphical representation (Discussion 6.3 helps us develop key insights into the plausible mechanisms for such observations. Furthermore, the whole rock REE content also provides an understanding of the key factors that control REE enrichment in black shale.

Table 6. Individual REE and Total REE concentrations in the organic leachate fraction.

| ID | Sc | Y | La | Ce | Pr | Nd | Sm | Eu | Gd | Tb | Dy | Ho | Er | Tm | Yb | Lu | TREY |
|----|-------|-------|-------|-------|-------|-------|-------|-------|-------|-------|-------|-------|-------|-------|-------|-------|-------|
| | mg/L |
| D1 | 0.396 | 0.162 | 1.036 | 2.160 | 0.327 | 1.432 | 0.188 | 0.028 | 0.112 | 0.013 | 0.065 | 0.013 | 0.038 | 0.005 | 0.026 | 0.004 | 6.004 |
| D1 | 0.303 | 0.221 | 0.556 | 1.344 | 0.219 | 1.053 | 0.137 | 0.022 | 0.087 | 0.013 | 0.065 | 0.013 | 0.039 | 0.005 | 0.028 | 0.005 | 4.110 |
| C3 | 0.177 | 0.083 | 0.431 | 1.051 | 0.178 | 0.698 | 0.069 | 0.013 | 0.055 | 0.007 | 0.036 | 0.007 | 0.019 | 0.002 | 0.014 | 0.002 | 2.842 |
| C2 | 0.071 | 0.076 | 0.404 | 1.133 | 0.178 | 0.610 | 0.056 | 0.011 | 0.047 | 0.006 | 0.040 | 0.008 | 0.022 | 0.003 | 0.014 | 0.002 | 2.682 |
| C1 | 0.127 | 0.148 | 0.285 | 0.777 | 0.125 | 0.482 | 0.068 | 0.016 | 0.072 | 0.010 | 0.061 | 0.012 | 0.032 | 0.004 | 0.021 | 0.002 | 2.241 |
| B | 0.206 | 0.247 | 0.361 | 0.963 | 0.167 | 0.664 | 0.078 | 0.019 | 0.081 | 0.014 | 0.078 | 0.015 | 0.044 | 0.005 | 0.035 | 0.005 | 2.980 |
| B | 0.129 | 0.161 | 0.534 | 1.294 | 0.208 | 0.729 | 0.080 | 0.016 | 0.080 | 0.000 | 0.058 | 0.010 | 0.031 | 0.004 | 0.024 | 0.003 | 3.359 |
| A2 | 0.049 | 0.087 | 0.403 | 0.706 | 0.084 | 0.249 | 0.037 | 0.010 | 0.041 | 0.000 | 0.030 | 0.006 | 0.015 | 0.002 | 0.012 | 0.001 | 1.735 |
| A2 | 0.061 | 0.074 | 0.279 | 0.409 | 0.050 | 0.157 | 0.027 | 0.008 | 0.030 | 0.000 | 0.024 | 0.005 | 0.015 | 0.002 | 0.014 | 0.002 | 1.158 |
| A1 | 0.018 | 0.055 | 0.154 | 0.169 | 0.025 | 0.103 | 0.025 | 0.007 | 0.029 | 0.000 | 0.020 | 0.003 | 0.009 | 0.001 | 0.005 | 0.000 | 0.623 |

6. Discussion

6.1. HREE Enrichment in Black Shale

The mineralogical changes down the stratigraphic column (Figure 3) clearly demonstrate that two lithological end members are present based on the silicate and carbonate contents in the chosen sequence with varying proportions of other minerals and TOC. The clay content is dominated by illite, which is as high as 60% in the upper D1 sample and gradually decreases as the units become increasingly calcareous. We see a similar trend with chlorite, although it disappears completely at the B–A2 transition. As for the carbonates (calcite, dolomite, and Fe-dolomite), they are present in low concentrations in the higher units and increase towards A1. We observe a sharp increase in calcite and dolomite in the C1 and C2 samples, indicating a change in the siliciclastic and clay input into the marine waters. Pyrite content varies concomitantly with OM from C1 to the base

of the sequence. This implies that higher OM productivity combined with anoxia primarily controls the mineralogical composition of the deeper shales.

Since the chemical fractionation of REE occurs in a predictable fashion that corresponds to their increasing atomic number, it is assumed that individual REE will behave similarly when partitioning into the various shale-forming minerals. This concept will help us substantiate the relationships we observe between HREE and TOC from the Middle Devonian rocks and kerogen isolates of global oil shales. Kerogen isolates, which are a concentrated form of organic carbon, can be useful to develop a mechanistic understanding of HREE partitioning in pure kerogen. Although the comparison is between two different kinds of samples, we argue that in both cases the focus lies on HREE association with organic matter components in black shales. Furthermore, Figure 5a,b also draw our attention to whether the thermal maturity of the shale has an influence on partitioning, as we see opposite HREE trends with increasing TOC contents. Therefore, it is reasonable to consider comparing the HREE data of the highly mature Middle Devonian samples with the relatively more immature kerogen samples of global oil shale. We note that there is a moderately positive trend in HREE with an increase in TOC in Figure 5a. This observation is in agreement with a few previous studies that propose that the HREE enrichment in the whole rock is contributed by organics [21]. On the contrary, the HREE content in kerogen isolates extracted from global oil shales (see Table 7) show an inverse relationship with TOC (Figure 5b). This opposite trend suggests that other factors besides TOC might be controlling the HREE partitioning; for example, it is possible that hydrocarbon-generating aliphatic organic moieties are not a repository for HREE. To corroborate the data, we assessed the relationship between TOC and certain redox-sensitive elements, such as V, Ni, Cu, Mo, and U in our Appalachian Basin samples.

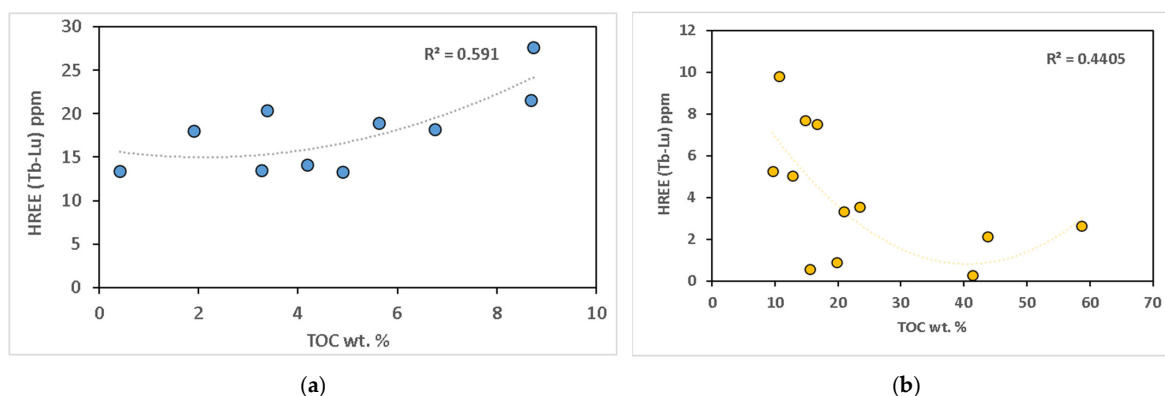


Figure 5. (a) HREE in overmature Middle Devonian shales. (b) HREE in kerogen isolate of immature global oil shales.

6.2. REE Distributions in Immature Oil Shales and Kerogen Isolates

The oil shale samples examined as part of this work represent a range of sedimentary rock formations from various basins around the world. All samples are thermally immature, based on maceral reflectance (vitrinite or solid bitumen), programmed pyrolysis parameters, and kerogen elemental ratios. The samples include examples from the Mahogany oil-shale zone of the Eocene Green River Formation (GR; Piceance Basin, CO, USA); Cretaceous Timahdit oil shale (TM; Morocco); Cretaceous Ghareb Formation (GI and GJ) shales from two locations (Israel and Jordan; sometimes referred to as the Muwaqqar Formation in Jordan); Jurassic Kimmeridgian Blackstone (KB; England); Permian Irati Formation marinite (IF; Brazil); Permian Glen Davis torbanite (GD; Australia); Permian shale of the Phosphoria Formation (PR; MT, USA); Carboniferous Pumpherstons torbanite (PO; Scotland); Mississippian–Devonian New Albany shale (NA; IN, USA); Ordovician Narva-E mine kukersite (EK; Estonia); and the Cambrian Alum Shale Formation (AS; Sweden).

Table 7. HREE content in global oil shales kerogen isolates (BRL = below reporting limit).

| Sample ID | Mineralogy | Y | La | Ce | Pr | Nd | Sm | Eu | Gd | Tb | Dy | Ho | Er | Tm | Yb | Lu | TREE | HREE |
|-----------|---------------------------|------|------|------|------|------|-----|------|-----|------|------|------|------|------|-----|------|-------|------|
| | | ppm | ppm | ppm | ppm | ppm | ppm | ppm | ppm | ppm | ppm | ppm | ppm | ppm | ppm | ppm | ppm | ppm |
| GR | Carbonate–quartz/feldspar | 7.5 | 8.9 | 14.4 | 1.56 | 4.6 | 0.7 | 0.13 | 0.6 | 0.16 | 1.03 | 0.24 | 0.79 | 0.15 | 1 | 0.18 | 34.46 | 2.12 |
| TM | ML clays–carbonate | 10.5 | 3 | 5.8 | 0.61 | 1.9 | 0.5 | 0.13 | 0.9 | 0.19 | 1.56 | 0.34 | 1.21 | 0.21 | 1.5 | 0.27 | 18.08 | 3.19 |
| GI | Carbonate | 1.4 | 0.8 | 1.7 | 0.19 | 0.6 | 0.1 | BRL | 0.1 | BRL | 0.21 | BRL | 0.15 | BRL | 0.2 | BRL | 4.05 | 0.35 |
| GJ | Carbonate–clay | 2 | 1 | 1.9 | 0.2 | 0.6 | 0.1 | BRL | 0.1 | BRL | 0.26 | 0.07 | 0.2 | BRL | 0.3 | 0.06 | 4.82 | 0.56 |
| KB | Claystone | 5 | 1.9 | 3.6 | 0.44 | 1.5 | 0.3 | 0.09 | 0.5 | 0.1 | 0.73 | 0.16 | 0.49 | 0.08 | 0.5 | 0.08 | 10.47 | 1.15 |
| IF | Quartz–illite | 22.9 | 19 | 35.1 | 4.22 | 15.4 | 3.4 | 0.66 | 3.8 | 0.7 | 4.05 | 0.76 | 2.02 | 0.31 | 1.7 | 0.29 | 91.39 | 4.32 |
| GD | Quartz | 7.3 | 0.5 | 0.9 | 0.11 | 0.5 | 0.1 | BRL | 0.1 | BRL | 0.54 | 0.18 | 0.72 | 0.14 | 0.9 | 0.16 | 4.88 | 1.92 |
| PR | Quartz–ML clays | 8.9 | 19 | 7.3 | 1.08 | 3.1 | 0.5 | 0.13 | 0.6 | 0.15 | 1.04 | 0.22 | 0.73 | 0.14 | 0.9 | 0.15 | 35.05 | 1.92 |
| PO | Quartz–kaolinite | 14.6 | 6.9 | 11.8 | 1.37 | 4.3 | 0.8 | 0.22 | 1.1 | 0.26 | 2.01 | 0.46 | 1.72 | 0.33 | 2.3 | 0.43 | 33.96 | 4.78 |
| NA | Quartz–illite | 18.3 | 6.5 | 11.3 | 1.22 | 4 | 0.9 | 0.27 | 1.8 | 0.41 | 2.86 | 0.6 | 1.73 | 0.27 | 1.6 | 0.23 | 33.73 | 3.83 |
| EK | Carbonate–clay | 1.3 | 0.6 | 1 | 0.16 | 0.6 | 0.1 | BRL | 0.2 | BRL | 0.18 | BRL | 0.09 | BRL | BRL | BRL | 2.91 | 0.09 |
| AS | Quartz–illite | 12.4 | 11.4 | 17.2 | 1.68 | 5.3 | 1.1 | 0.27 | 1.5 | 0.28 | 1.89 | 0.4 | 1.15 | 0.16 | 1 | 0.16 | 43.47 | 2.47 |

These elements demonstrate a distinct mineralogical dependence as the rock TOC content increases downward from C1 (Figure 6). Between B and A1, the sharp increase in the trace metal concentration coincides with an increase in TOC from 3–9.5 wt.%. V, Ni, Cu, Mo, and U vary from about 80–280 ppm, 0–150 ppm, 0–130 ppm, 20–100 ppm, and 0–15 ppm in the upper sections, respectively, and to about 280–640 ppm, 150–370 ppm, 130–280 ppm, 60–150 ppm, and 30–60 ppm in the lower sections, respectively. This increase in elemental concentrations relates directly to the associated reduction in dissolved oxygen concentrations with depth [19,21,32,42,90]. As the REE demonstrate a similar response to a change in redox with depth (Figure 6), we therefore use the HREE data reliably to understand its relationship with TOC. A study on Utica Shale magnafacies in Quebec, Ontario, and New York shows that REE in the organic fraction represents up to almost 20% of the whole rock content [18]. Abanda and Hannigan (2006) [18] reported that the elemental association with OM was much higher than with the sulfide or carbonate fraction. The trend of HREE distribution in our samples also supports that organics can play a key role in controlling the whole rock REE content, in addition to the silicate fraction. To verify the trend, it is necessary to find visible HREE enrichment patterns, which is evident in Figure 4.

It is important to consider other factors in addition to the role of OM that could influence the LREE-HREE enrichment pattern in the whole rocks. We see a variation in the mildly negative Ce anomalies and that can likely be attributed to differences in the extent of biologically mediated activities at particular depths (Figure 4). We hypothesize that local disturbances in the pore waters may have affected the redox conditions and influenced the oxidation of Ce and the growth of microbial communities. More negative anomalies in the deeper stratigraphic horizon would suggest persistent anoxia during the deposition of A1 [20] that prevented the formation of discrete CeO₂ grains. However, it is difficult to resolve if the same biological mediation was responsible for simultaneous Mn-oxide formation or if the degrees of oxidation are controlled by a common process [20]. It is also important to note that although we have a reasonable understanding of the modes of REE partitioning during sediment–fluid interactions in marine settings, most of these studies have been conducted on immature shales. Therefore, the published geochemical models do not consider the effects of thermal alteration on REE distribution in black shales and this is why it is challenging to adequately interpret the REE patterns of the highly mature samples in our study.

The cross plot of the Y concentration against the TOC content in our samples shows that there is a non-linear positive trend in Y with an increase in TOC (Figure 7). This observation aligns with a study by Fuchs et al. (2016) [40] that focused on metal and REE occurrences in pyrobitumen. They reported significantly higher amounts of Y in pyrobitumen (mean concentration of 600 ppm) relative to the mineral matrix of black shales. It is known that Y is an abundant mineral in xenotime and in the interstices of pyrobitumen nodules, and it may also be present either in the structure or occur as nanoparticles. The higher Y content may invariably be a function of pyrobitumen formation during thermal maturation. This suggests that HREE in general tend to be more concentrated in pyrobitumen than the LREE, regardless of the variations in lithology.

Based on the whole rock pattern and moderately strong positive correlation between Y and TOC, we argue that pyrobitumen is potentially the primary host of the heavier lanthanides. Several studies have reported that an increase in shale porosity with increasing thermal maturity is associated strongly with changes in the porosity within OM [91–97]. The lanthanides can hence be incorporated either in OM-hosted pores or in the pyrobitumen structure. A study by Chen and Xiao (2014) [98] evaluated the evolutionary characteristics of OM-hosted nanoporosity in artificially matured shales. It was found that vitrinite reflectance has a strong control on the meso-, micro- and nanopore development within the thermally evolving OM. Therefore, careful evaluation is warranted to determine the nature of association of HREE with pyrobitumen, as that has implications for the development of extraction techniques.

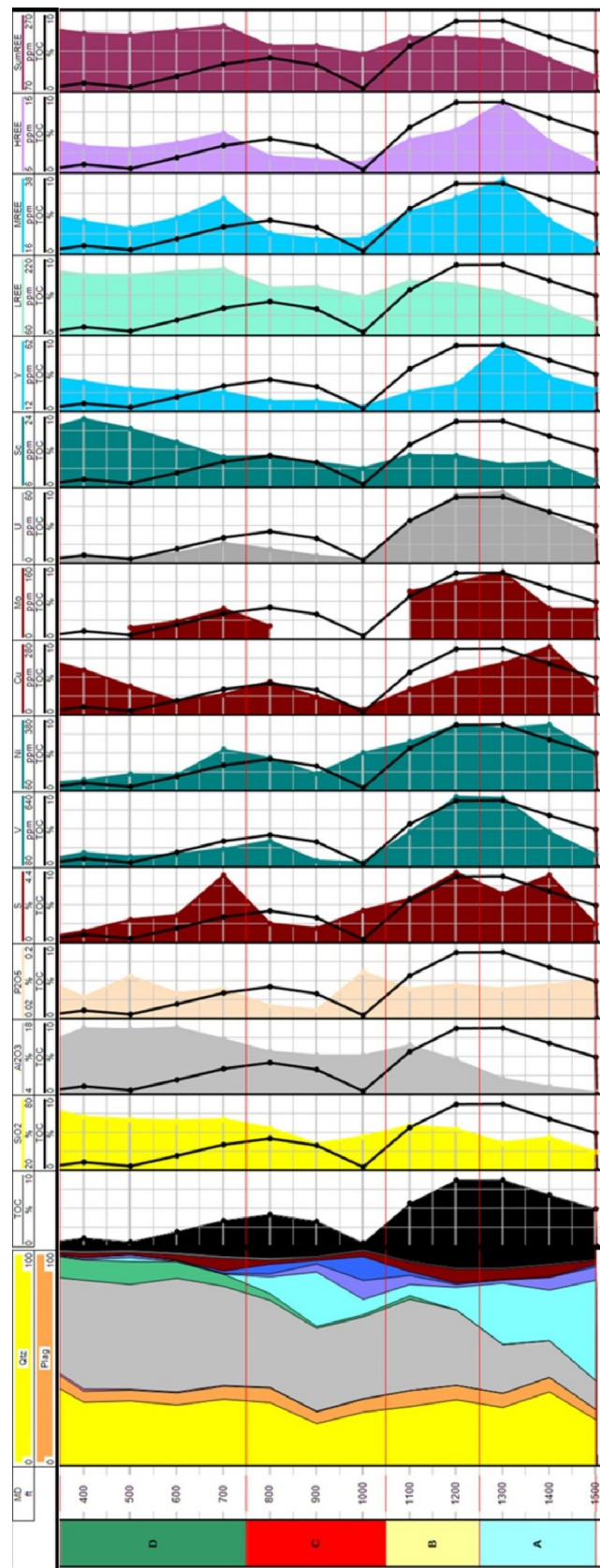


Figure 6. A comparative illustration to track the covariance of redox sensitive parameters, namely, sulfur, TOC.

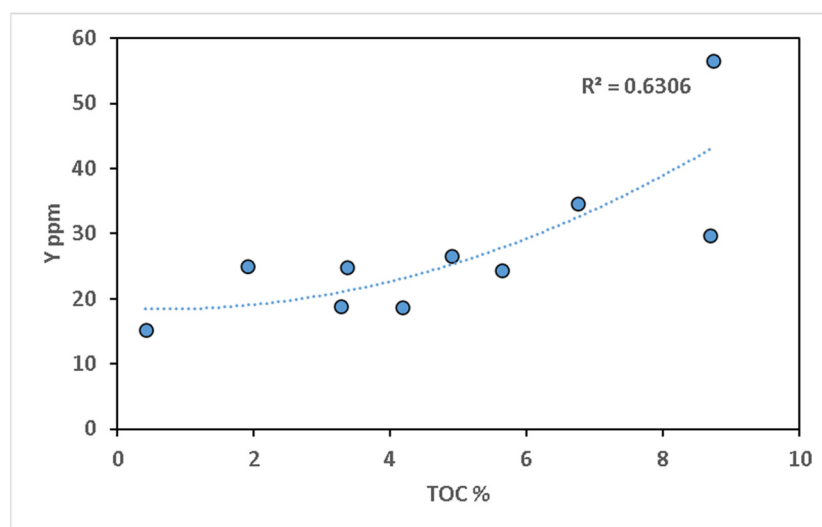


Figure 7. Increasing Y with TOC in whole rock.

Devonian black shales in the Appalachian Basin have been extensively studied with respect to the thermal maturity, mineral assemblages, and nature of OM. In highly mature and overmature rocks (>3% VRo), similar to our Appalachian samples studied here, the dominating OM identified is pyrobitumen [99–101]. Photomicrographs and the 3D modeling of the Marcellus Formation from our Appalachian samples used in this study confirm the presence of thermally altered organics in the form of highly aromatic pyrobitumen (cannot be published for proprietary reasons). Furthermore, the presence of sub-greenschist metamorphic facies and prehnite-pumpellyite assemblage allude to post-mature Devonian shales in highly mature parts of the basin. This corroborates that the highly mature shales contain higher OM porosity compared with those at lower maturities in the wet-gas window. These highly mature regions of the Marcellus basin contain an organic network that may also preserve conditions favorable for the existence of tetrapyrrolic and porphyrin complexes of HREE, including Y. This supports our hypothesis that overmature OM is the primary repository of heavy lanthanides. Therefore, the HREE-enriched pattern in the whole rock (Figure 4) and the positive correlation between TOC and HREE (Figure 5a) demonstrate the role of OM in the incorporation of REE distribution.

6.3. REE Partitioning during Chemical Leaching of OM

To ensure that all the REE were effectively leached from the organic fraction, the sample was combusted at 650 °C for 3.5 h to concentrate them as rare earth oxides prior to rinsing with diluted acid. Subsequently, a Leco TOC analysis was performed to verify if all the OM had been removed at the combustion step, which showed that OM was efficiently removed during the experiment (see Figure S1 in Supplementary Materials). The PAAS-normalized REE pattern indicates that the REE are significantly depleted in the organic leachate fraction. OM was completely removed except for two A samples (Figure 8). Hence, the REE volume in the organic leachate is a true representation of the total REE likely associated with the pyrobitumen solubilized with an acid in the whole rock.

This is, however, contradictory to our expectation that the organic leachates from our extractions show higher relative concentrations of lighter REEs instead of the heavier ones that are known to be present in higher concentrations in OM in the whole rock (Figures 5a and 6). This observation suggests that while OM has an affinity for HREE, it is also more challenging to decouple them using traditional leaching techniques. We hypothesize that nanoscopic specks of apatite, and potentially, xenotime, embedded in OM-hosted pores could be responsible for generating positive Y anomalies in the whole rock but negative anomalies in the organic leachates. The REE abundance also drastically decreased from Tb, indicating that Dy and Ho, which are conventionally grouped into MREE, are

observed to behave similar to the HREE. We also saw similar distribution patterns in the whole rock, indicating that there is some similarity in the MREE and HREE distribution patterns (Figure 4). We propose that this warrants a reevaluation of REE classifications based on the objectives of the study. For the purpose of understanding the cause of poor recoveries from our samples, grouping Tb, Y, Dy, Ho, Er, Tm, Yb, and Lu as HREE was determined to be a reasonable way to evaluate HREE behavior in mature black shales. Furthermore, Tb and Y could not be extracted from the high-TOC samples, suggesting these two elements behave similarly as the other HREE, and therefore the PAAS-normalized Y and Tb ratios could be reliable indicators of the behavior of HREE in overmatured rocks. A similar anomalous behavior of Y and Tb has been reported previously [6]. The soluble OM, which was extracted via the traditional leaching procedure, mobilized the lighter rare earth elements, because LREE are known to be incompatible elements. It is important to reiterate that the samples are overmatured and that the likelihood of residual soluble OM is expected to be very low. Since our OM removal was successful, as seen from the Leco TOC analysis of the residue, we propose a few mechanisms that corroborate our data. First, some fraction of the TOC is composed of labile hydrocarbons that were not expelled at the time of thermal maturation and had retained the LREE volume that was generated during leaching. We also assume that the soluble OM may have been trapped by association with refractory silicates during remineralization [37] and that is plausibly the primary source of the remnant LREE in organic leachates. The second mechanism explains the presence of low LREE by accounting for significant loss during processes such as kerogen cracking, the migration of oil, and oil cracking. These three processes are progressive stages of thermal maturation [102]. Therefore, a highly mature shale is expected to be significantly depleted in LREE. Thirdly, to account for the HREE enrichment, we attribute it to the formation of thermally resistant stable organic compounds (discussed in detail previously), which made LREE less likely to be preserved in OM. Therefore, the whole rock and leachate REE patterns agree with our hypothesis that although OM has a higher affinity for HREE, thermal maturity plays a more critical role in determining the modes of REE occurrence.

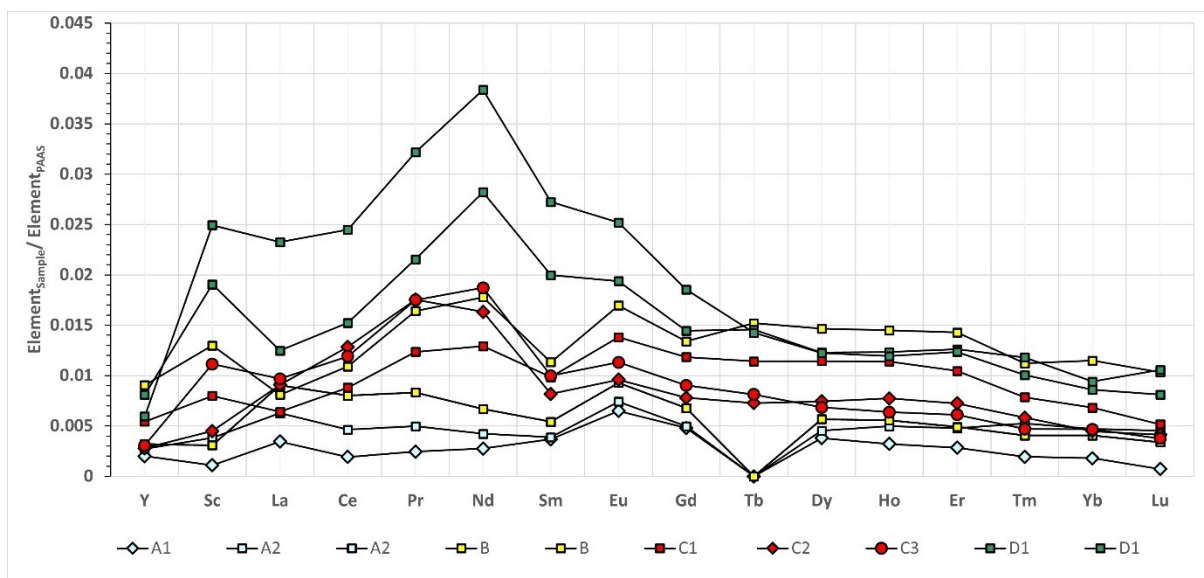


Figure 8. PAAS-normalized REE abundances in the organic leachate fraction.

6.4. Geochemical Model for REE Incorporation in Mature Organic-Rich Shale

The current understanding of REE partitioning during the thermal maturation of black shales is limited. There can be several modes of occurrence depending not only on the source but also on the post-burial diagenetic processes and the presence of authigenic minerals or lack thereof. Since we do not find the occurrence of minerals that have an

affinity for rare earth elements, we focused our geochemical model to role of OM and siliciclastics, excluding carbonates and sulfides.

The hypothetical model can be divided into depositional and post-depositional processes and can be described as follows:

Depositional stage: During a high influx of organic material from various sources into the marine waters, dissolved REE in seawater [20,103,104] is scavenged by carboxyl groups of humic acids during the early stages of OM deposition. As the depth in the water column increases, there is a relative increase in HREE over LREE due to the increasing stability of complexes with an increase in the atomic number of the lanthanides. Therefore, depositing OM preferentially takes up more HREE. With compaction, there is a release of REE into pore waters due to the reductive dissolution of Fe–Mn oxyhydroxides [105–108] that may further increase the possibility of the REE to be incorporated into OM.

Post-depositional stage: After compaction is complete, and when thermal maturation reaches a point that initiates a release of aggressive pore fluids from OM and the dewatering of smectite to forms illitic clays, there is a further preferential partitioning of HREE into the solid OM. Other processes that can mobilize HREE are through the formation of stable tetrapyrrolic and porphyrin complexes which are tenacious at high temperatures and resistant to cation exchange reactions. When oil is released due to maturation, these compounds migrate into nano- and micropores from the origin along the temperature gradient. As maturation progresses from the oil to wet gas and then dry gas, there is significant modification of OM-hosted shale porosity. While fluids remain in the evolving shale system, certain organic networks develop which may host a fraction of the rare earths, preferentially retaining the heavy REE, simultaneously depleting the host rock in LREE. At further stages of maturation, there is cracking of oil, leading to the generation of gas and pyrobitumen. With the expulsion of oil, a volume of LREE may be lost and the stable tetrapyrroles are preserved in thermally recalcitrant pyrobitumen, which may later become partially graphitized at higher temperatures. This sequence of events can ultimately give rise to a HREE-enriched pattern that we observe in all the high TOC-rich samples. On the other hand, the negative correlation between HREE and TOC in the relatively immature oil shales may be attributed to the lack of significant thermal maturation resulting in the preferential retention of HREEs in organic residues not occurring.

7. Conclusions

We conclude that organic matter in highly matured black shales plays a significant role in partitioning and remobilizing heavy rare earths. The opposite trends between global oil shales and over-matured Middle Devonian shales with respect to the relationship between TOC and HREE help develop the idea that thermal maturation process is an important factor to consider when studying geochemical behavior of REE association. It is therefore likely that although TOC has a control on REE enrichment relative to PAAS, thermal maturity is the most important factor that governs HREE partitioning into refractory materials, such as pyrobitumen.

- We established an REE inventory from the D1 through A1. The total REE ranges from 180 to 270 ppm and the OM-rich samples tend to contain more REE than the calcareous shales.
- The samples show a relatively higher abundance of middle and heavy REEs than light REEs.
- There is a disproportionate increase in Y and Tb with TOC, suggesting these elements are more strongly bound to OM and thus can be used in tracer studies.
- The organic leachates from our experiments contained more LREE than HREE despite the HREE concentration being higher in OM. This observation suggests that while OM has an affinity for HREE, it also is more challenging to decouple them using traditional leaching techniques. The high Y and Tb content in the whole rock reflects that the HREE are incorporated under high thermal conditions and these elements can be used

as reliable proxies for determining nature of refractory OM in highly mature black shales.

The REE in pore waters and their marine sediment counterparts can exhibit a wide range of REE concentrations controlled by different redox conditions, diagenetic environments, and thermal maturation. Therefore, this study shows the need to further explore shales from other basins and the effects of other maturation processes on the geochemical behavior of REE. Our preliminary findings contribute to the development of a better understanding of the role of maturation history, the scavenging capacity of pyrobitumen, and the potential role of clays in the remobilization of REE from the silicates. Finally, building an REE inventory in other major shale plays could help tap into unconventional REE resources to meet the global demands of these relevant elements.

Supplementary Materials: The following supporting information can be downloaded at: <https://www.mdpi.com/article/10.3390/en17092107/s1>. Figure S1: Comparative illustration to track the mineralogical changes in the residual samples after leaching. Figure S2: Ternary plots for mineralogical proportions of the samples. Table S1: Method Detection limits; Table S2: Cerium and Europium anomalies in the whole rock; Table S3: Formation location of global oil shales.

Author Contributions: Conceptualization: S.B., V.A. and S.S.; Supervision: S.S.; Formal Analysis: S.S., M.C.D. and G.Z.; Conducted the experiments: S.B. and V.A.; Visualization: M.C.D. and S.B.; Writing original draft: S.B.; Edited the manuscript: S.B., S.S., V.A., M.C.D., J.E.B., G.Z., T.W. and A.S.W.J.; Resources: S.S. and T.W. All authors have read and agreed to the published version of the manuscript.

Funding: This research was funded by Coterra Energy Inc. Oil shale and kerogen work was funded by the U.S. Geological Survey Energy Resources Program. Publication of this article was supported by the John C. Ludlum Geology Endowment, Department of Geology and Geography, West Virginia University, Morgantown.

Data Availability Statement: Concentration data (lanthanide and related elements) for oil shale whole rock and kerogen samples available in a U.S. Geological survey data release [109] on [ScienceBase.gov](https://sciencebase.gov).

Conflicts of Interest: The authors declare no conflicts of interest. M.C.D., G.Z. were employed by Premier Corex Laboratories and W.T. were employed by the company Coterra Energy Inc. The remaining authors declare that the research was conducted in the absence of any commercial or financial relationships that could be construed as a potential conflict of interest.

References

1. Arnold, B.J. A review of element partitioning in coal preparation. *Int. J. Coal Geol.* **2023**, *274*, 104296. [[CrossRef](#)]
2. Wang, Q.; Chen, X.; Jha, A.N.; Rogers, H. Natural gas from shale formation—the evolution, evidences and challenges of shale gas revolution in United States. *Renew. Sustain. Energy Rev.* **2014**, *30*, 1–28. [[CrossRef](#)]
3. Considine, T.; Watson, R.; Blumsack, S. *The Economic Impacts of the Pennsylvania Marcellus Shale Natural Gas Play: An Update*; The Pennsylvania State University, Department of Energy and Mineral Engineering: State College, PA, USA, 2010.
4. Phan, T.T.; Hakala, J.A.; Lopano, C.L.; Sharma, S. Rare earth elements and radiogenic strontium isotopes in carbonate minerals reveal diagenetic influence in shales and limestones in the Appalachian Basin. *Chem. Geol.* **2019**, *509*, 194–212. [[CrossRef](#)]
5. Yang, J.; Torres, M.; McManus, J.; Algeo, T.J.; Hakala, J.A.; Verba, C. Controls on rare earth element distributions in ancient organic-rich sedimentary sequences: Role of post-depositional diagenesis of phosphorus phases. *Chem. Geol.* **2017**, *466*, 533–544. [[CrossRef](#)]
6. Bhattacharya, S.; Agrawal, V.; Sharma, S. Association of Rare Earths in Different Phases of Marcellus and Haynesville Shale: Implications on Release and Recovery Strategies. *Minerals* **2022**, *12*, 1120. [[CrossRef](#)]
7. Scott, C.; Slack, J.F.; Kelley, K.D. The hyper-enrichment of V and Zn in black shales of the Late Devonian-Early Mississippian Bakken Formation (USA). *Chem. Geol.* **2017**, *452*, 24–33. [[CrossRef](#)]
8. Freslon, N.; Bayon, G.; Toucanne, S.; Bermell, S.; Bollinger, C.; Chéron, S.; Etoubleau, J.; Germain, Y.; Khripounoff, A.; Ponzevera, E.; et al. Rare earth elements and neodymium isotopes in sedimentary organic matter. *Geochim. Cosmochim. Acta* **2014**, *140*, 177–198. [[CrossRef](#)]
9. Elderfield, H.; Greaves, M.J. The rare earth elements in seawater. *Nature* **1982**, *296*, 214–219. [[CrossRef](#)]
10. Elderfield, H. The oceanic chemistry of the rare-earth elements. *Philos. Trans. R. Soc. Lond. Ser. A Math. Phys. Sci.* **1988**, *325*, 105–126.
11. Sholkovitz, E.; Ronald, S. The estuarine chemistry of rare earth elements: Comparison of the Amazon, Fly, Sepik and the Gulf of Papua systems. *Earth Planet. Sci. Lett.* **2000**, *179*, 299–309. [[CrossRef](#)]

12. Milodowski, A.E.; Zalasiewicz, J.A. Redistribution of rare earth elements during diagenesis of turbidite/hemipelagite mudrock sequences of Llandovery age from central Wales. *Geol. Soc. Lond. Spec. Publ.* **1991**, *57*, 101–124. [[CrossRef](#)]
13. Goldberg, E.D.; Koide, M.; Schmitt, R.A.; Smith, R.H. Rare-Earth distributions in the marine environment. *J. Geophys. Res.* **1963**, *68*, 4209–4217. [[CrossRef](#)]
14. Byrne, R.H.; Sholkovitz, E.R. Marine chemistry and geochemistry of the lanthanides. *Handb. Phys. Chem. Rare Earths* **1996**, *23*, 497–593.
15. Wood, S.A. The aqueous geochemistry of the rare-earth elements and yttrium: 1. Review of available low-temperature data for inorganic complexes and the inorganic REE speciation of natural waters. *Chem. Geol.* **1990**, *82*, 159–186. [[CrossRef](#)]
16. Millero, F.J. Stability constants for the formation of rare earth-inorganic complexes as a function of ionic strength. *Geochim. Cosmochim. Acta* **1992**, *56*, 3123–3132. [[CrossRef](#)]
17. Lee, J.H.; Byrne, R.H. Examination of comparative rare earth element complexation behavior using linear free-energy relationships. *Geochim. Cosmochim. Acta* **1992**, *56*, 1127–1137. [[CrossRef](#)]
18. Abanda, P.A.; Hannigan, R.E. Effect of diagenesis on trace element partitioning in shales. *Chem. Geol.* **2006**, *230*, 42–59. [[CrossRef](#)]
19. Haley, B.A.; Klinkhammer, G.P.; McManus, J. Rare earth elements in pore waters of marine sediments. *Geochim. Cosmochim. Acta* **2004**, *68*, 1265–1279. [[CrossRef](#)]
20. Moffett, J.W. Microbially mediated cerium oxidation in sea water. *Nature* **1990**, *345*, 421–423. [[CrossRef](#)]
21. Klinkhammer, G.; Heggge, D.T.; Graham, D.W. Metal diagenesis in oxic marine sediments. *Earth Planet. Sci. Lett.* **1982**, *61*, 211–219. [[CrossRef](#)]
22. Moldowan, J.M.; Sundararaman, P.; Schoell, M. Sensitivity of biomarker properties to depositional environment and/or source input in the Lower Toarcian of SW-Germany. *Org. Geochem.* **1986**, *10*, 915–926. [[CrossRef](#)]
23. Ten Haven, H.L.; De Leeuw, J.W.; Peakman, T.M.; Maxwell, J.R. Anomalies in steroid and hopanoid maturity indices. *Geochim. Cosmochim. Acta* **1986**, *50*, 853–855. [[CrossRef](#)]
24. Ten Haven, H.L.; De Leeuw, J.W.; Damsté, J.S.S.; Schenck, P.A.; Palmer, S.E.; Zumberge, J.E. Application of biological markers in the recognition of palaeohypersaline environments. *Geol. Soc. Lond. Spec. Publ.* **1988**, *40*, 123–130. [[CrossRef](#)]
25. Curiale, J.A.; Odermatt, J.R. Short-term biomarker variability in the Monterey Formation, Santa Maria basin. *Org. Geochem.* **1989**, *14*, 1–13. [[CrossRef](#)]
26. Strachan, R.A.; Smith, M.; Harris, A.L.; Fettes, D.J. *The Northern Highland and Grampian Terranes*; Geological Society of London: London, UK, 2002.
27. Dahl, I.M.; Kolboe, S. On the reaction mechanism for propene formation in the MTO reaction over SAPO-34. *Catal. Lett.* **1993**, *20*, 329–336. [[CrossRef](#)]
28. Snowdon, L.R. Rock-Eval Tmax suppression: Documentation and amelioration. *AAPG Bull.* **1995**, *79*, 1337–1348.
29. French, K.L.; Hallmann, C.; Hope, J.M.; Schoon, P.L.; Zumberge, J.A.; Hoshino, Y.; Peters, C.A.; George, S.C.; Love, G.D.; Brocks, J.J.; et al. Reappraisal of hydrocarbon biomarkers in Archean rocks. *Proc. Natl. Acad. Sci. USA* **2015**, *112*, 5915–5920. [[CrossRef](#)] [[PubMed](#)]
30. French, K.; Birdwell, J.; Berg, V. Biomarker similarities between the saline lacustrine eocene green river and the paleoproterozoic Barney Creek Formations. *Geochim. Cosmochim. Acta* **2020**, *274*, 228–245. [[CrossRef](#)]
31. Kidder, D.L.; Krishnaswamy, R.; Mapes, R.H. Elemental mobility in phosphatic shales during concretion growth and implications for provenance analysis. *Chem. Geol.* **2003**, *198*, 335–353. [[CrossRef](#)]
32. Lev, S.M.; McLennan, S.M.; Hanson, G.N. Mineralogic controls on REE mobility during black-shale diagenesis. *J. Sediment. Res.* **1999**, *69*, 1071–1082. [[CrossRef](#)]
33. Awwiller, D.N. Illite/smectite formation and potassium mass transfer during burial diagenesis of mudrocks; a study from the Texas Gulf Coast Paleocene-Eocene. *J. Sediment. Res.* **1993**, *63*, 501–512.
34. Bloch, J.; Hutcheon, I.E. Shale Diagenesis: A Case Study from the Albian Harmon Member (Peace River Formation), Western Canada. *Clays Clay Miner.* **1992**, *40*, 682–699. [[CrossRef](#)]
35. Raiswell, R.; Berner, R.A. Organic carbon losses during burial and thermal maturation of normal marine shales. *Geology* **1987**, *15*, 853–856. [[CrossRef](#)]
36. Miknis, F.P.; Jiao, Z.S.; MacGowan, D.B.; Surdam, R.C. Solid-state NMR characterization of Mowry shale from the Powder River Basin. *Org. Geochem.* **1993**, *20*, 339–347. [[CrossRef](#)]
37. Tait, L. *The Character of Organic Matter and the Partitioning of Trace and Rare Earth Elements in Black Shales; Blondeau Formation, Chibougamau, Québec*; Université du Québec à Chicoutimi: Chicoutimi, QC, Canada, 1987.
38. Chen, Z.; Simoneit, B.R.; Wang, T.-G.; Ni, Z.; Yuan, G.; Chang, X. Molecular markers, carbon isotopes, and rare earth elements of highly mature reservoir pyrobitumens from Sichuan Basin, southwestern China: Implications for PreCambrian-Lower Cambrian petroleum systems. *Precambrian Res.* **2018**, *317*, 33–56. [[CrossRef](#)]
39. Mastalerz, M.; Glikson, M. In-situ analysis of solid bitumen in coal: Examples from the Bowen Basin and the Illinois Basin. *Int. J. Coal Geol.* **2000**, *42*, 207–220. [[CrossRef](#)]
40. Fuchs, S.; Williams-Jones, A.E.; Jackson, S.E.; Przybyłowicz, W.J. Metal distribution in pyrobitumen of the Carbon Leader Reef, Witwatersrand Supergroup, South Africa: Evidence for liquid hydrocarbon ore fluids. *Chem. Geol.* **2016**, *426*, 45–59. [[CrossRef](#)]
41. Martynov, A.G.; Horii, Y.; Katoh, K.; Bian, Y.; Jiang, J.; Yamashita, M.; Gorbunova, Y.G. Rare-earth based tetrapyrrolic sandwiches: Chemistry, materials and applications. *Chem. Soc. Rev.* **2022**, *51*, 9262–9339. [[CrossRef](#)] [[PubMed](#)]

42. Lewan, M.D.; Maynard, J.B. Factors controlling enrichment of vanadium and nickel in the bitumen of organic sedimentary rocks. *Geochim. Cosmochim. Acta* **1982**, *46*, 2547–2560. [[CrossRef](#)]
43. Hodgson, G.W.; Baker, B.L. Vanadium, nickel, and porphyrins in thermal geochemistry of petroleum. *AAPG Bull.* **1957**, *41*, 2413–2426.
44. Rosscup, R.J.; Bowman, D.H. Thermal Stabilities of Vanadium and Nickel Porphyrins. *Div. Pet. Chem. Am. Chem. Soc.* **1967**, *12*, 77.
45. Caughy, W.S.; Corwin, A.H. The Stability of Metalloetioporphyrins toward Acids1. *J. Am. Chem. Soc.* **1955**, *77*, 1509–1513. [[CrossRef](#)]
46. Dean, R.A.; Girdler, R.B. Reaction of metal etioporphyrins on dissolution in sulfuric acid. *Chem. Indust.* **1960**, 100–101.
47. Barnes, J.W.; Dorough, G.D. Exchange and Replacement Reactions of α , β , γ , δ -Tetraphenyl-metalloporphyrins1. *J. Am. Chem. Soc.* **1950**, *72*, 4045–4050. [[CrossRef](#)]
48. Corwin, A.H. Petroporphyrins. In Proceedings of the 5th World Petroleum Congress, New York, NY, USA, 30 May–5 June 1959; Section V. pp. 120–129.
49. Dunning, H.N.; Moore, J.W.; Denekas, M.O. Interfacial activities and porphyrin contents of petroleum extracts. *Ind. Eng. Chem.* **1953**, *45*, 1759–1765. [[CrossRef](#)]
50. Erdman, J.G.; Walter, J.W.; Hanson, W.E. The stability of the porphyrin metallo complexes. *Amer. Chem. Soc. Div. Petrol. Chem. Prepr.* **1957**, *2*, 259–267.
51. Fleischer, E.B. The structure of nickel etioporphyrin-I. *J. Am. Chem. Soc.* **1963**, *85*, 146–148. [[CrossRef](#)]
52. Jiang, J.; Ng, D.K.P. A decade journey in the chemistry of sandwich-type tetrapyrrolo– rare earth complexes. *Acc. Chem. Res.* **2009**, *42*, 79–88. [[CrossRef](#)]
53. Jiang, J.; Bian, Y.; Furuya, F.; Liu, W.; Choi, M.T.M.; Kobayashi, N.; Li, H.-W.; Yang, Q.; Mak, T.C.W.; Ng, D.K.P. Synthesis, Structure, Spectroscopic Properties, and Electrochemistry of Rare Earth Sandwich Compounds with Mixed 2, 3-Naphthalocyaninato and Octaethylporphyrinato Ligands. *Chem. A Eur. J.* **2001**, *7*, 5059–5069. [[CrossRef](#)]
54. Pushkarev, V.E.; Tomilova, L.G.; Nemykin, V.N. Historic overview and new developments in synthetic methods for preparation of the rare-earth tetrapyrrolic complexes. *Coord. Chem. Rev.* **2016**, *319*, 110–179. [[CrossRef](#)]
55. Lysenko, A.B.; Malinovskii, V.L.; Padmaja, K.; Wei, L.; Diers, J.R.; Bocian, D.F.; Lindsey, J.S. Multistate molecular information storage using S-acetylthio-derivatized dyads of triple-decker sandwich coordination compounds. *J. Porphyr. Phthalocyanines* **2005**, *9*, 491–508. [[CrossRef](#)]
56. Ali, M.F.; Abbas, S. A review of methods for the demetallization of residual fuel oils. *Fuel Process. Technol.* **2006**, *87*, 573–584. [[CrossRef](#)]
57. Brongersma-Sanders, M. On conditions favouring the preservation of chlorophyll in marine sediments. In Proceedings of the World Petroleum Congress, The Hague, The Netherlands, 28 May–6 June 1951; p. WPC-4027.
58. Gorham, E.; Sanger, J. Plant pigments in woodland soils. *Ecology* **1967**, *48*, 306–308. [[CrossRef](#)]
59. Drozdova, T.V.; Gorskiy, Y.N. Conditions of preservation of chlorophyll, pheophytin and humic matter in Black Sea sediments. *Geokhimiya* **1972**, *3*, 323–334.
60. He, R.; Lu, W.; Junium, C.K.; Straeten, C.A.V.; Lu, Z. Paleo-redox context of the Mid-Devonian Appalachian Basin and its relevance to biocrises. *Geochim. Cosmochim. Acta* **2020**, *287*, 328–340. [[CrossRef](#)]
61. Brett, C.E.; Baird, G.C.; Bartholomew, A.J.; DeSantis, M.K.; Straeten, C.A.V. Sequence stratigraphy and a revised sea-level curve for the Middle Devonian of eastern North America. *Palaeogeogr. Palaeoclimatol. Palaeoecol.* **2011**, *304*, 21–53. [[CrossRef](#)]
62. Ver Straeten, C.A.; Brett, C.E.; Sageman, B.B. Mudrock sequence stratigraphy: A multi-proxy (sedimentological, paleobiological and geochemical) approach, Devonian Appalachian Basin. *Palaeogeogr. Palaeoclimatol. Palaeoecol.* **2011**, *304*, 54–73. [[CrossRef](#)]
63. Ver Straeten, C.; Baird, G.; Brett, C.; Lash, G.; Over, J.; Karaca, C.; Jordan Blood, R. The Marcellus Subgroup in its type area, Finger Lakes area of New York, New York State Geological Association Field Guide. In Proceedings of the 83rd Annual Meeting, 14–16 October 2011; pp. 23–86.
64. Stein, W.E.; Mannolini, F.; Hernick, L.V.; Landing, E.; Berry, C.M. Giant cladoxylous trees resolve the enigma of the Earth’s earliest forest stumps at Gilboa. *Nature* **2007**, *446*, 904–907. [[CrossRef](#)] [[PubMed](#)]
65. Ettensohn, F.R.; Miller, M.L.; Dillman, S.B.; Elam, T.D.; Geller, K.L.; Swager, D.R.; Markowitz, G.; Woock, R.D.; Barron, L.S. *Characterization and Implications of the Devonian-Mississippian Black Shale Sequence, Eastern and Central Kentucky, USA: Pycnoclines, Transgression, Regression, and Tectonism*; AAPG: Tulsa, OK, USA, 1988; pp. 323–345.
66. Woodrow, D.L.; Dennison, J.M.; Ettensohn, F.R.; Sevon, W.T.; Kirchgasser, W.T. *Middle and Upper Devonian Stratigraphy and Paleogeography of the Central and Southern Appalachians and Eastern Midcontinent, USA*; AAPG: Tulsa, OK, USA, 1988; pp. 277–301.
67. Ettensohn, F.R.; Barron, L.S. Tectono-climatic model for origin of Devonian-Mississippian black gas shales of east-central United States. *AAPG Bull.* **1981**, *65*, 923.
68. Chen, R.; Sharma, S. Linking the Acadian Orogeny with organic-rich black shale deposition: Evidence from the Marcellus Shale. *Mar. Pet. Geol.* **2017**, *79*, 149–158. [[CrossRef](#)]
69. Ettensohn, F.R. Modeling the nature and development of major Paleozoic clastic wedges in the Appalachian Basin, USA. *J. Geodyn.* **2004**, *37*, 657–681. [[CrossRef](#)]
70. Murphy, A.E.; Sageman, B.B.; Hollander, D.J.; Lyons, T.W.; Brett, C.E. Black shale deposition and faunal overturn in the Devonian Appalachian Basin: Clastic starvation, seasonal water-column mixing, and efficient biolimiting nutrient recycling. *Paleoceanography* **2000**, *15*, 280–291. [[CrossRef](#)]

71. Werne, J.P.; Sageman, B.B.; Lyons, T.W.; Hollander, D.J. An integrated assessment of a “type euxinic” deposit: Evidence for multiple controls on black shale deposition in the Middle Devonian Oatka Creek Formation. *Am. J. Sci.* **2002**, *302*, 110–143. [[CrossRef](#)]
72. Sageman, B.B.; Murphy, A.E.; Werne, J.P.; Straeten, C.A.V.; Hollander, D.J.; Lyons, T.W. A tale of shales: The relative roles of production, decomposition, and dilution in the accumulation of organic-rich strata, Middle–Upper Devonian, Appalachian basin. *Chem. Geol.* **2003**, *195*, 229–273. [[CrossRef](#)]
73. Algeo, T.J. Can marine anoxic events draw down the trace element inventory of seawater? *Geology* **2004**, *32*, 1057–1060. [[CrossRef](#)]
74. Rimmer, S.M. Geochemical paleoredox indicators in Devonian–Mississippian black shales, central Appalachian Basin (USA). *Chem. Geol.* **2004**, *206*, 373–391. [[CrossRef](#)]
75. Gordon, G.W.; Lyons, T.W.; Arnold, G.L.; Roe, J.; Sageman, B.B.; Anbar, A.D. When do black shales tell molybdenum isotope tales? *Geology* **2009**, *37*, 535–538. [[CrossRef](#)]
76. Lash, G.G.; Blood, D.R. Organic matter accumulation, redox, and diagenetic history of the Marcellus Formation, southwestern Pennsylvania, Appalachian basin. *Mar. Pet. Geol.* **2014**, *57*, 244–263. [[CrossRef](#)]
77. Blood, D.R.; Lash, G.G.; Larsen, D.; Egenhoff, S.O.; Fishman, N.S. Dynamic redox conditions in the Marcellus Shale as recorded by pyrite framboid size distributions. *Paying Atten. Mudrocks Priceless* **2015**, *515*, 153–168.
78. Chen, R.; Sharma, S. Role of alternating redox conditions in the formation of organic-rich interval in the Middle Devonian Marcellus Shale, Appalachian Basin, USA. *Palaeogeogr. Palaeoclimatol. Palaeoecol.* **2016**, *446*, 85–97. [[CrossRef](#)]
79. Blakey, R. Global Paleogeography. 2005. Available online: <http://jan.ucc.nau.edu/~rcb7/globaltext2.html> (accessed on 24 September 2009).
80. Ver Straeten, C.A. Microstratigraphy and depositional environments of a middle Devonian foreland basin: Berne and Otsego members, Mount Marion formation, eastern New York state. *Stud. Stratigr. Paleontol. Honor Donald W. Fish. N. Y. State Mus. Bull.* **1994**, *481*, 367–380.
81. Straeten, C.A.V.; Brett, C.E. Pragian to Eifelian strata (middle Lower to lower Middle Devonian), northern Appalachian Basin—stratigraphic nomenclatural changes. *Northeast. Geol. Environ. Sci.* **2006**, *28*, 80.
82. Ver Straeten, C.A. Basinwide stratigraphic synthesis and sequence stratigraphy, upper Pragian, Emsian and Eifelian stages (Lower to Middle Devonian), Appalachian Basin. *Geol. Soc. Lond. Spec. Publ.* **2007**, *278*, 39–81. [[CrossRef](#)]
83. Engelder, T.; Lash, G.G.; Uzcátegui, R.S. Joint sets that enhance production from Middle and Upper Devonian gas shales of the Appalachian Basin. *AAPG Bull.* **2009**, *93*, 857–889. [[CrossRef](#)]
84. U.S. EPA. *Method 200.7: Determination of Metals and Trace Elements in Water and Wastes by Inductively Coupled Plasma-Atomic Emission Spectrometry*; U.S. EPA: Cincinnati, OH, USA, 1994; Revision 4.4.
85. U.S. EPA. *Method 200.8: Determination of Trace Elements in Waters and Wastes by Inductively Coupled Plasma-Mass Spectrometry*; U.S. EPA: Cincinnati, OH, USA, 1994; Revision 5.4.
86. Lewan, M.D.; Bjørøy, M.; Dolcater, D.L. Effects of thermal maturation on steroid hydrocarbons as determined by hydrous pyrolysis of Phosphoria Retort Shale. *Geochim. Cosmochim. Acta* **1986**, *50*, 1977–1987. [[CrossRef](#)]
87. USGS Mineral Resources Program. Method 18—Sixty Elements by Inductively Coupled Plasma-Optical Emission Spectroscopy-Mass Spectrometry (ICP-OES-MS), Sodium Peroxide Fusion (ICP-60). 2018. Available online: <https://www.usgs.gov/media/files/60-elements-icp-oes-ms-na2o-fusion-method> (accessed on 15 April 2022).
88. Pourmand, A.; Dauphas, N.; Ireland, T.J. A novel extraction chromatography and MC-ICP-MS technique for rapid analysis of REE, Sc and Y: Revising CI-chondrite and Post-Archean Australian Shale (PAAS) abundances. *Chem. Geol.* **2012**, *291*, 38–54. [[CrossRef](#)]
89. De Baar, H.J.W.; Bacon, M.P.; Brewer, P.G. Rare-earth distributions with a positive Ce anomaly in the Western North Atlantic Ocean. *Nature* **1983**, *301*, 324–327. [[CrossRef](#)]
90. Kim, J.-H.; Torres, M.E.; Haley, B.A.; Kastner, M.; Pohlman, J.W.; Riedel, M.; Lee, Y.-J. The effect of diagenesis and fluid migration on rare earth element distribution in pore fluids of the northern Cascadia accretionary margin. *Chem. Geol.* **2012**, *291*, 152–165. [[CrossRef](#)]
91. Ross, D.J.K.; Bustin, R.M. Shale gas potential of the lower Jurassic Gordondale member, northeastern British Columbia, Canada. *Bull. Can. Pet. Geol.* **2007**, *55*, 51–75. [[CrossRef](#)]
92. Ross, D.J.K.; Bustin, R.M. Characterizing the shale gas resource potential of Devonian–Mississippian strata in the Western Canada sedimentary basin: Application of an integrated formation evaluation. *AAPG Bull.* **2008**, *92*, 87–125. [[CrossRef](#)]
93. Chalmers, G.R.L.; Bustin, R.M. The organic matter distribution and methane capacity of the Lower Cretaceous strata of Northeastern British Columbia, Canada. *Int. J. Coal Geol.* **2007**, *70*, 223–239. [[CrossRef](#)]
94. Chalmers, G.R.L.; Bustin, R.M. Lower Cretaceous gas shales in northeastern British Columbia, Part I: Geological controls on methane sorption capacity. *Bull. Can. Pet. Geol.* **2008**, *56*, 1–21. [[CrossRef](#)]
95. Valenza, J.J.; Drenzek, N.; Marques, F.; Pagels, M.; Mastalerz, M. Geochemical controls on shale microstructure. *Geology* **2013**, *41*, 611–614. [[CrossRef](#)]
96. Carroll, A.R. Upper Permian lacustrine organic facies evolution, southern Junggar Basin, NW China. *Org. Geochem.* **1998**, *28*, 649–667. [[CrossRef](#)]
97. Milliken, K.L.; Rudnicki, M.; Awwiller, D.N.; Zhang, T. Organic matter-hosted pore system, Marcellus formation (Devonian), Pennsylvania. *AAPG Bull.* **2013**, *97*, 177–200. [[CrossRef](#)]

98. Chen, J.; Xiao, X. Evolution of nanoporosity in organic-rich shales during thermal maturation. *Fuel* **2014**, *129*, 173–181. [[CrossRef](#)]
99. Laughrey, C.D. Produced Gas and Condensate Geochemistry of the Marcellus Formation in the Appalachian Basin: Insights into Petroleum Maturity, Migration, and Alteration in an Unconventional Shale Reservoir. *Minerals* **2022**, *12*, 1222. [[CrossRef](#)]
100. Laughrey, C.D.; Lemmens, H.; Ruble, T.E.; Butcher, A.R.; Walker, G.; Kostelnik, J.; Barnes, J.; Knowles, W. Black shale diagenesis: Insights from integrated high-definition analyses of post-mature Marcellus Formation rocks, northeastern Pennsylvania. In *Critical Assessment of Shale Resource Plays*; AAPG: Tulsa, OK, USA, 2013; AAPG Memoir 103.
101. Delle Piane, C.; Bourdet, J.; Josh, M.; Clennell, M.B.; Rickard, W.D.A.; Saunders, M.; Sherwood, N.; Li, Z.; Dewhurst, D.N.; Raven, M.D. Organic matter network in post-mature Marcellus Shale: Effects on petrophysical properties. *AAPG Bull.* **2018**, *102*, 2305–2332. [[CrossRef](#)]
102. Tissot, B.P.; Welte, D.H. *Petroleum Formation and Occurrence*, 2nd ed.; Springer: Berlin/Heidelberg, Germany, 1984; p. 699.
103. Sholkovitz, E.R.; Landing, W.M.; Lewis, B.L. Ocean particle chemistry: The fractionation of rare earth elements between suspended particles and seawater. *Geochim. Cosmochim. Acta* **1994**, *58*, 1567–1579. [[CrossRef](#)]
104. Hathorne, E.C.; Stichel, T.; Brück, B.; Frank, M. Rare earth element distribution in the Atlantic sector of the Southern Ocean: The balance between particle scavenging and vertical supply. *Mar. Chem.* **2015**, *177*, 157–171. [[CrossRef](#)]
105. Klinkhammer, G.P.; Elderfield, H.; Edmond, J.M.; Mitra, A. Geochemical implications of rare earth element patterns in hydrothermal fluids from mid-ocean ridges. *Geochim. Cosmochim. Acta* **1994**, *58*, 5105–5113. [[CrossRef](#)]
106. Douville, E.; Charlou, J.L.; Oelkers, E.H.; Bienvenu, P.; Colon, C.F.J.; Donval, J.P.; Fouquet, Y.; Prieur, D.; Appriou, P. The rainbow vent fluids (36°14' N, MAR): The influence of ultramafic rocks and phase separation on trace metal content in Mid-Atlantic Ridge hydrothermal fluids. *Chem. Geol.* **2002**, *184*, 37–48. [[CrossRef](#)]
107. Tostevin, R.; Wood, R.A.; Shields, G.A.; Poulton, S.W.; Guilbaud, R.; Bowyer, F.; Penny, A.M.; He, T.; Curtis, A.; Hoffmann, K.H.; et al. Low-oxygen waters limited habitable space for early animals. *Nat. Commun.* **2016**, *7*, 12818. [[CrossRef](#)]
108. Sensarma, S.; Saha, A.; Hazra, A. Implications of REE incorporation and host sediment influence on the origin and growth processes of ferromanganese nodules from Central Indian Ocean Basin. *Geosci. Front.* **2021**, *12*, 101123. [[CrossRef](#)]
109. Birdwell, J.E. *Rare Earth Element Concentrations for Oil Shales and Isolated Kerogens from around the world: U.S. Geological Survey Data Release*; U.S. Geological Survey: Reston, VA, USA, 2024. [[CrossRef](#)]

Disclaimer/Publisher’s Note: The statements, opinions and data contained in all publications are solely those of the individual author(s) and contributor(s) and not of MDPI and/or the editor(s). MDPI and/or the editor(s) disclaim responsibility for any injury to people or property resulting from any ideas, methods, instructions or products referred to in the content.